Does Relative Rotation Inclination Affect Disk Lifetime in Young Binaries?

By Lauren I. Biddle

A Thesis

Submitted in Partial Fulfillment

of the Requirements for the Degree of

Master of Science

in Applied Physics

Northern Arizona University

May 2017

Approved:

Lisa Prato, Ph.D., Chair

David Koerner, Ph.D.

David Cole, Ph.D.

Abstract

Surveys show strong evidence that disks typically dissipate in ∼5 Myr, therefore planets must form on a similar timescale. However, the primary mechanisms driving disk-loss are still under investigation. Young binary stars are ideal targets for studying disk evolution because their stellar component provides a small control sample. This study probes the possibility that the relative rotation axes' inclinations of young binaries may significantly affect disk lifetime, thus impacting their ability to form planets. A case study of the young binary DF Tau combines observational and computational analyses to investigate component rotation axes' inclinations and compare them to the circumstellar disk properties of this system. Periodogram analyses of unresolved time-series photometry recover a rotation period of 10.5 d for the primary and an upper limit of 3.3 d for the secondary. Rotation periods combined with spectrally-derived projected rotation velocities yield an inclination of 90 degrees for both components. Additional investigation into a strong 9.3 d period present in periodogram indicates accretion hot spots are likely the source. DF Tau is one example target selected from a sample of ∼100 different young binary observations and highlights the importance this data set has on informing our understanding of disk evolution and planet formation.

Acknowledgements

I would like to thank the following people:

Dr. Lisa Prato, committee chair

Dr. David Koerner, committee member

Dr. David Cole, committee member

Brian Skiff, for observations and valuable insight

My family and friends, for their continuous support.

Contents

List of Tables

List of Figures

Dedication

To my mom, dad, sister, and brother.

Chapter 1

Introduction

The formation and evolution of a circumstellar disk is a vital step in stellar evolution–perhaps the most fundamental of astrophysical processes that ultimately dictates the nature of planet-forming systems. The complexity of the problem can be broken down into a sequence of evolutionary stages (Figure 1.1, Shu et al., 1987). The process begins within a giant molecular cloud, a diffuse and irregular collection of gas and dust, which forms self-gravitating, massive concentrations of matter in cold cores. These cores eventually become unstable and collapse under their own gravity to form a spherical mass supported by thermal hydrostatic equilibrium known as a protostar. Protostars are characteristically embedded in an envelope of infalling accreting material and surrounded by optically thick disks; part of the envelope is eventually ejected in high-energy bipolar outflows. However, the remaining matter continues to drive the evolutionary process as the once-encompassing envelope accretes onto the circumstellar disk. The disk itself accretes onto the now optically revealed pre-main sequence (PMS) object, most commonly referred to as a T Tauri star (TTS). The last stage of stellar evolution is the disappearance of the circumstellar disk and the emergence onto the main sequence as a potentially planet-hosting star.

The prominent mechanism(s) behind disk-dispersal during the PMS evolutionary

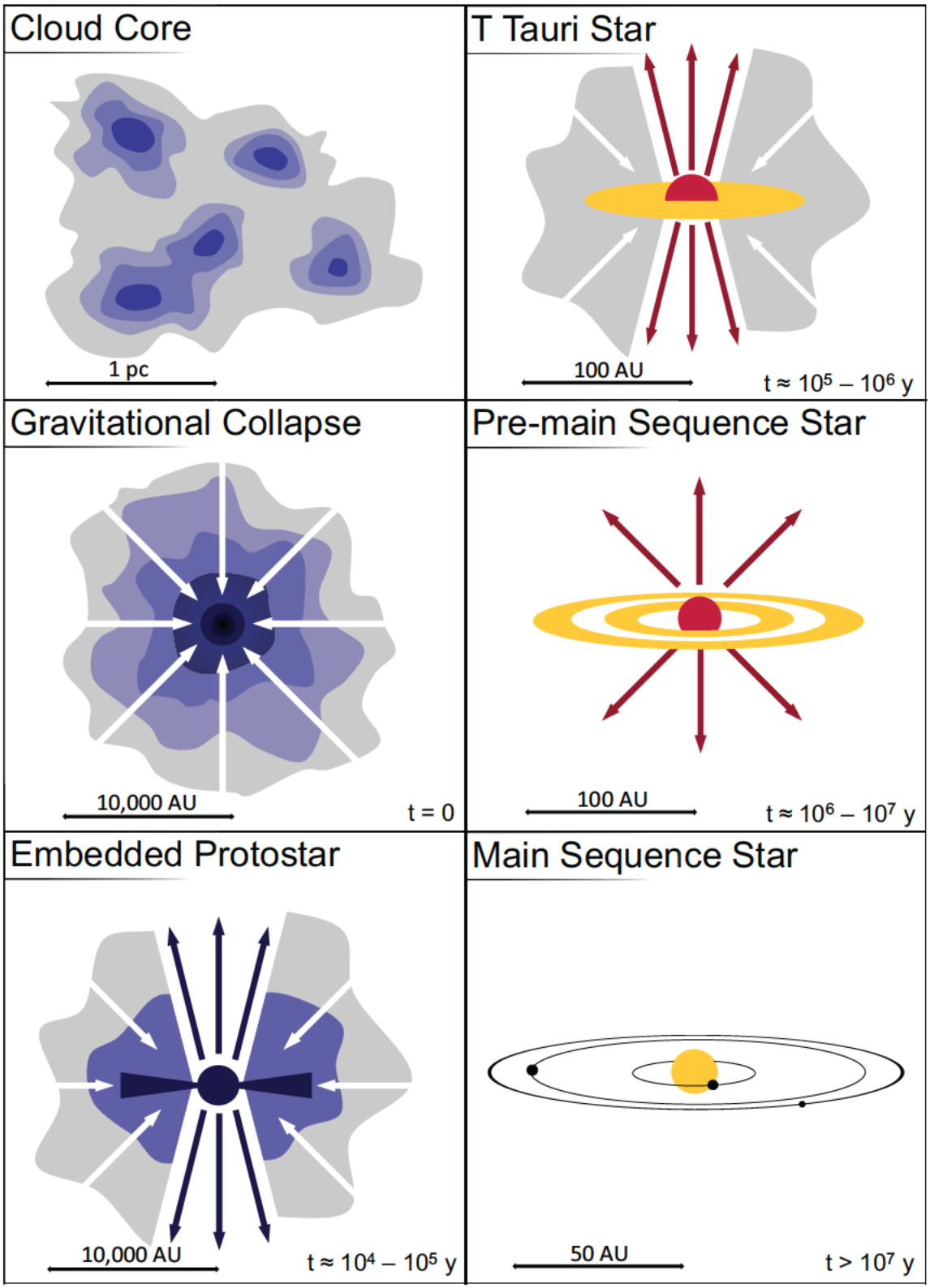

Figure 1.1: Cartoon representation of the evolutionary steps of star and planet formation.

phase is not a well-understood phenomenon. Observationally, circumstellar disks that may yet undergo, or are actively engaging in, planet formation are hosted by TTS. TTS are extremely young (0.1-10 Myr), low-mass (0.1-1.0$M_{\odot}$) objects that fall into roughly two classifications: (1) classical T Tauri stars (CTTS), which show evidence of hosting an optically thick circumstellar disk and exhibit varying amounts of star-disk magnetic and dynamical interactions such as disk-locking and accretion (Bertout et al., 1988), and (2) weak-line T Tauri stars (WTTS), which have also not yet evolved onto the main sequence, but do not demonstrate significant mass accretion and show no indication of an inner disk (Walter, 1987). It is thought that WTTS may be the evolutionary product of CTTS because statistical surveys suggest circumstellar disks are likely to dissipate in $\lesssim$ 5 Myr into their lifetime (Hernández et al., 2007)(Figure 1.2). Understanding the interplay between CTTS and their disks is critical to our comprehension of what drives the disks' evolution (potentially through the WTTS phase) toward becoming planet-hosting main sequence stars.

The goal of this study is to use time-series photometry of TTS to help identify periodic signals that may be the result of flux modulation induced by giant spots on a rapidly rotating star, as well as potential sources of aperiodic variability that may help characterize mass accretion rates, outflow activity, and additional important processes such as occultations resulting from disk inhomogeneities. A likely ubiquitous source of variability among all young stars is the effect of cool spots on a star's observed photospheric flux, which provides a direct probe of a star's rotation period. Rotation periods provide a basic snapshot of the state of a star's angular momentum during its evolution into a main sequence star. Magnetic interactions (Figure 1.3) between a young star and even a small fraction of ionized gas in a disk regulate stellar rotation by "locking" the star into a state of co-rotation with inner edge of the disk (Stassun et al., 2000; Cauley et al., 2012). The star will spin up as it contracts upon the eventual dissipation of the disk. If CTTS in fact do evolve into WTTS, it would

then be expected that WTTS typically rotate more quickly than CTTS. However, recent evidence (Figure 1.4) suggests there is a difference in rotation periods among stars that differ in age but no statistically significant difference in rotation period between CTTS and WTTS (Karim et al., 2016). Although this is consistent with the prediction that TTS lose their inner disk at ∼5 Myr, the results show inconsistencies in the hypothesis that CTTS evolve into WTTS and spin up.

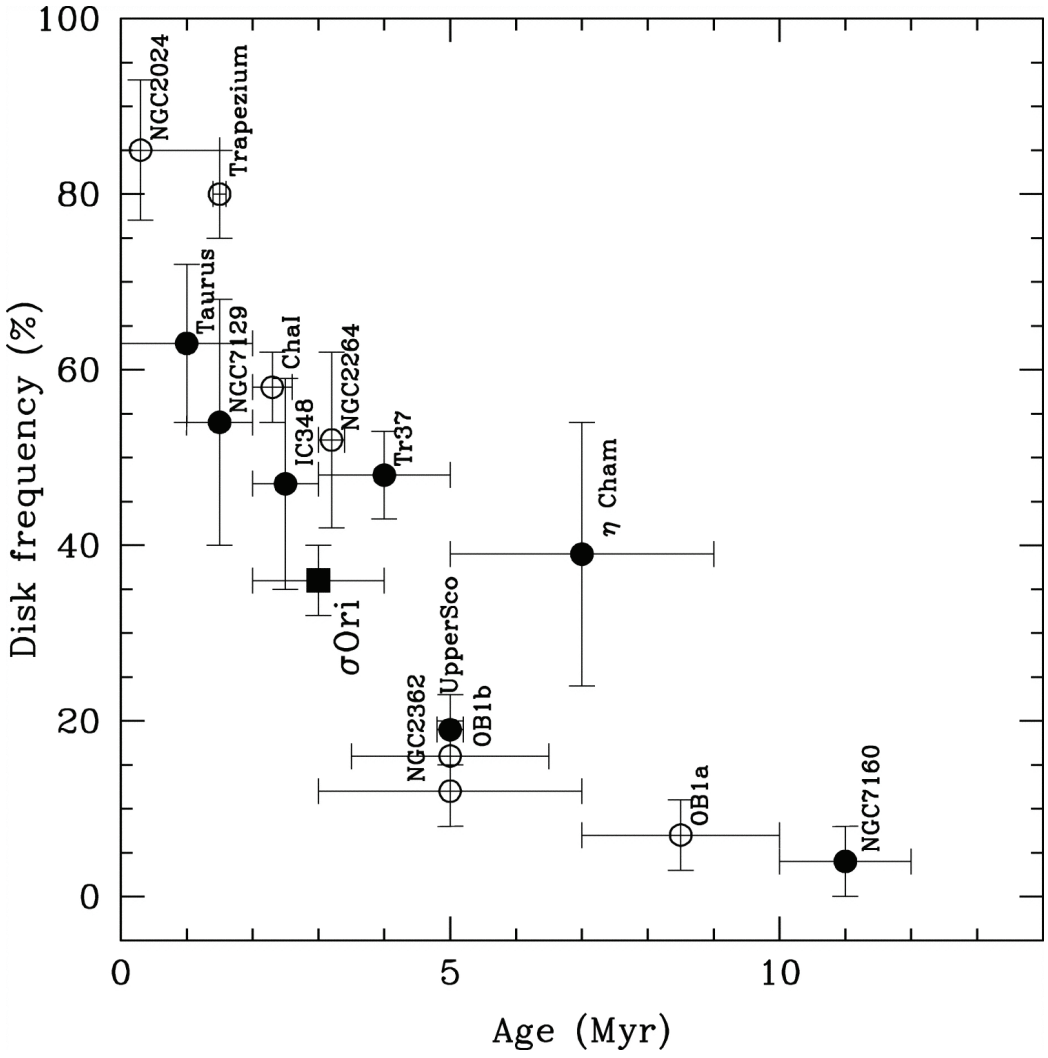

Figure 1.2: Disk frequency vs. age of young stellar clusters may provide an indication of the typical disk lifetime (Hernández et al., 2007). Filled symbols represent values calculated using IRAC data for stars in the PMS mass range (0.1-1.0$M_{\odot}$), and open symbols represent those determined with JKHL observations.

Acquiring optical photometry that clearly indicates rotational modulation is most

straightforward for WTTS because in the absence of a disk, interpretation of the nature of their variability is more straightforward (Grankin et al., 2008; Rigon et al., 2017). In contrast, the rotation periods of Classical T Tauri stars (CTTS) can be difficult to obtain because the behavior of the variability is predominantly irregular and can overshadow potential signals caused by rotational modulation. The most notable characteristic of CTTS is they are coupled to an accretion disk, so the most likely explanation for this sporadic variability is primarily the result of mass accretion onto the star. Hotspots on the photosphere caused by magnetospheric accretion can sometimes contribute to or confuse flux rotational modulation; however, they are relatively short-lived and typically dissipate within a few rotation periods (Herbst et al., 2007). As a result, fewer rotation periods of CTTS have been successfully recovered compared to those of WTTS, highlighting the importance of characterizing the source of short and long-term variations of CTTS.

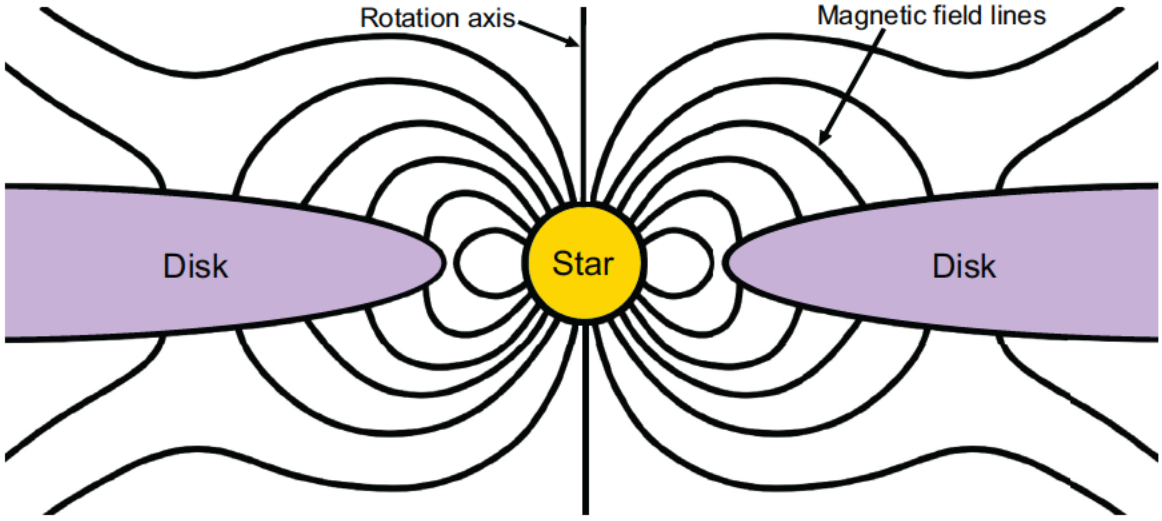

Figure 1.3: A cartoon depicting a simplified rotation axis-aligned magnetic field linking a star and disk.

Although photometry alone can provide useful insight into various properties of CTTS, it becomes a more powerful tool for recovering rotational inclination when coupled with spectroscopy. Spectra are essentially a record of a star's chemical footprint, which can provide not only its general composition, but also clues into its mass,

temperature, spectral type, magnetic field strength, radial velocity, and projected rotational velocity ($v \sin i$). When analyzed together, photometric and spectroscopic data can be used to provide evidential support for *or* against potential causes of an observed periodic signal. For example, starspots lead to variability in the photospheric absorption lines used to determine stellar radial velocity and can introduce periodicity, which may by misinterpreted as arising in radial velocity (RV) motion. To best interpret the photometry analyzed in this work, a combination of spectra and time-series photometry are analyzed together to disentangle observational degeneracies such as stellar equatorial rotation velocity (v) and inclination (i) in spectral measurements of $v \sin i$.

Young visual (angular sep > 0.04 arcsec, the diffraction limit of the worlds largest telescope, the 10 meter Keck, at 1.6 μm) binary and multiple stars are excellent laboratories for studying stellar and disk evolution because their companion stars provide a control sample. Also, most stars in the galaxy are a part of multiple-component systems (Raghavan et al., 2010), emphasizing the importance of understanding circumstellar disk lifetimes for binaries in particular. One consequence of binarity is the possibility for a stellar companion to disrupt the disk around the other star, which will affect the lifetime and/or morphology of the disk(s) (Cieza et al., 2009; Kraus et al., 2016). Artymowicz and Lubow (1994) theorized that for close binary systems, stability of a disk requires a radial upper limit 1/3 of the stars' orbital separation. However this is under the assumption that both stars' rotational axes are perpendicular to the orbital plane and parallel with each other. We do not know whether non-zero relative rotational inclinations of binary stars have a significant affect on disk lifetime. It is possible to investigate this if the relative rotational inclinations are known and the presence of a disk around one or both components is known.

This work focuses on one peculiar TTS system in the Taurus star forming region: DF Tau, a young visual binary with only one component that shows evidence of

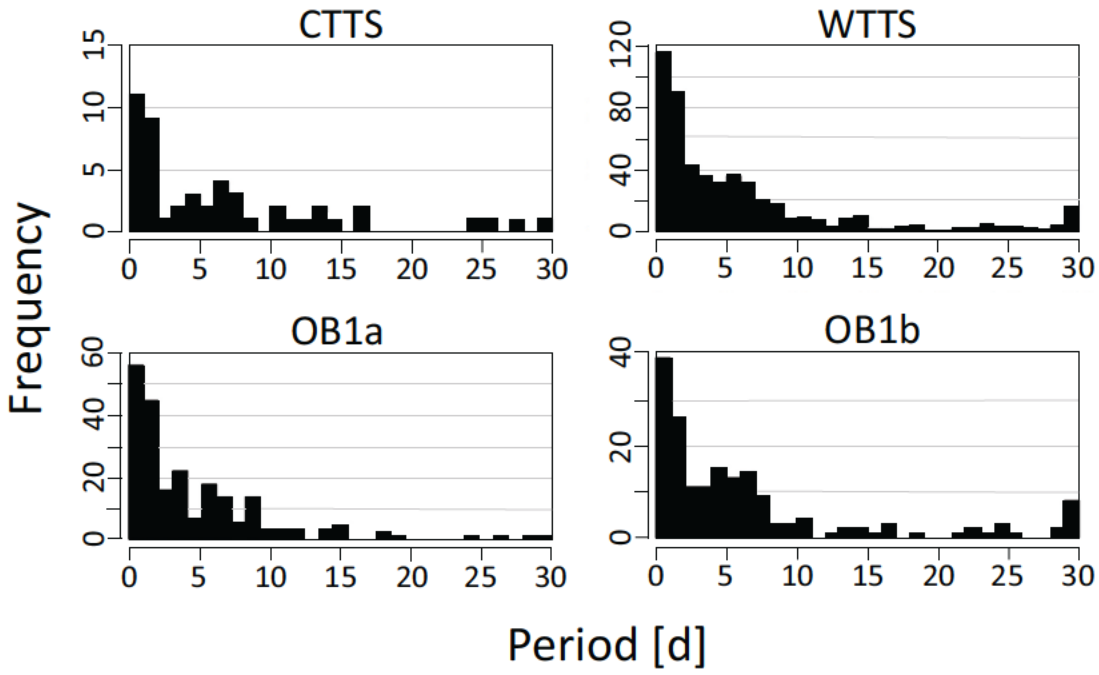

Figure 1.4: Distribution of young star rotation periods (Karim et al., 2016). *Top*: Rotation period distribution of CTTS and WTTS with mean periods of 6.87 d and 5.84 d, respectively. The authors perform an Anderson-Darling test on the CTTS and WTTS distributions and find no significant difference in rotation period. *Bottom*: Rotation period distribution of TTS in Orion OB1a and OB1b associations. TTS in OB1a (aged ∼10 Myr) have mean period of 4.37 d, and TTS in OB1b (aged ∼4 Myr) and have a mean period of 6.98 d. The same test performed on the period distributions of stars in OB1a and OB1b associations yields the result at 97.5% confidence that younger TTS rotate slower than older TTS.

having a circumstellar disk even though both stars are coeval and of the same mass. DF Tau is worth studying in detail because it possesses the advantages that come with belonging to a multiple star system– its properties can help illuminate disk-dissipation processes and can be interpreted without the assumption WTTS are a product of CTTS.

Chapter 2

Methodology

2.1 Observations

2.1.1 Time-Series Photometry

We acquired unresolved BVI photometry of DF Tau using the Lowell Observatory 0.7-m f/8 telescope in robotic mode. The CCD camera provides a 15 × 15″ field at an image-scale of 0″.9/pixel. The system was observed on 35 nights over four months between 2015 November 1 and 2016 February 28 UT. The field was visited up to five times each night. Exposures were 180, 60, and 20 seconds in the B, V, and I filters, respectively.

We used the commercial software Canopus (version 10.4.0.6) to perform standard photometric reductions, with bias and flat-field correction followed by ordinary differential aperture photometry. The diameter of the photometry apertures were typically 15″ depending on the nightly image quality. We adopted BVI magnitudes for the three comparison stars from the wide-field photometric surveys ASAS-3 (Pojmanski, 1997), TASS MkIV (Droege et al., 2006), and APASS DR9 (Henden, 2016), VizieR item II/336. These adjust the photometric zero-points close to the standard system. Interplay of the variable emission lines in DF Tau's spectrum, comparison

stars' colors, and passbands of the filters + CCD system will inevitably cause small zero-point shifts in magnitude. However, the magnitudes are nevertheless comparable to long-term means in all three filters.

2.1.2 High-Resolution Spectroscopy

Our team acquired spatially resolved spectroscopic observations of the DF Tau using NIRSPEC (McLean et al., 1998, 2000) aided by the adaptive optics (AO) system (NIRSPAO) on the Keck II 10 meter telescope. Observations were acquired on 2009 December 6, 2010 December 12, and 2013 December 13 UT (Figure 2.1). The NIRSPAO 2-pixel slit was $0.027 \times 2''.3$, and produced spectra (R =30,000) in order 49 (with a central wavelength of 1.555 μm). This order was used for analysis because of the lack of telluric absorption lines as well as the abundance of atomic and molecular lines (Mace et al., 2012). Dark frames, flat-field frames, and arc-lamp frames were obtained to correct for dark current, nonuniform pixel-to-pixel detector response and wavelength calibration. Target observations were made with an AB nodding pattern at two locations along the slit. The integration time for each nod was 300 seconds, and internal Ne, Ar, Xe, and Kr comparison lamps were used for wavelength calibration.

The data were reduced using REDSPEC (Kim et al., 2015), which utilizes routines for the spatial rectification, wavelength calibration, removal of detector, atmospheric and optical path artifacts, and extraction of spectra. The 2D spectra were rectified by 3rd order polynomial fits to the spatial dimensions and 2nd order polynomial fit to the spectral dimensions. We used comparison-lamp emission lines in order to determine the wavelength solution. Any instrumental fringing and bad pixels were removed. Two Gaussians were fit to each pixel of the spectral profile in the cross-dispersion direction to extract the individual component spectra. Further observing details are provided in Schaefer et al. (2012). The spectra were normalized to unity and were

barycentric-corrected.

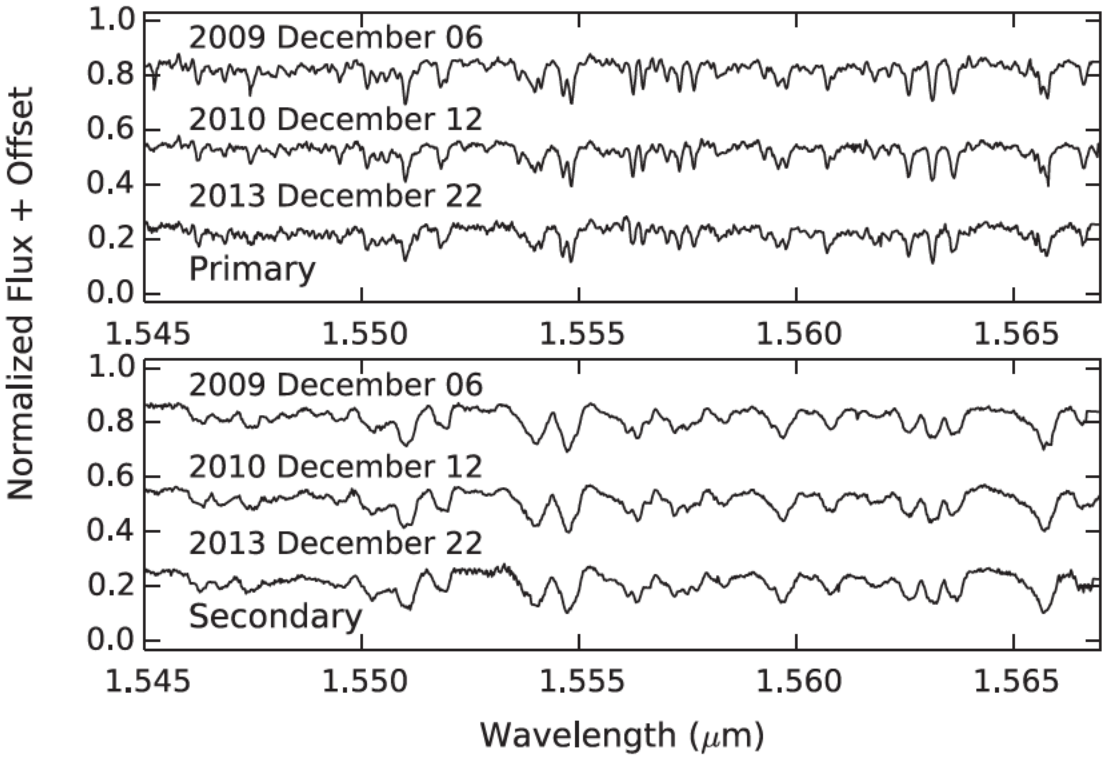

Figure 2.1: Resolved spectra of DF Tau components (Allen et al., 2017).

2.2 Analysis

2.2.1 Lomb-Scargle (L-S) Periodogram

In astronomy, recovering unknown periodic signals is common practice—especially in the field of stellar physics. However, due to the variability of weather conditions and ground-based telescope time allocation, it is uncommon for astronomers to acquire uniformly sampled data for which there are standard methods available to identify periodicity (e.g., Fast Fourier Transform). Thus, many astronomers must to rely on alternative methods designed to overcome this obstacle. One of the most common tools for extracting and analyzing periodic signals from unevenly sampled data is the classical Lomb-Scargle periodogram (CLS) (Scargle, 1982). This type of analysis

provides an analytic solution equivalent to fitting sine waves to time-series data (t_i, y_i with $\bar{y} = 0$) of the form $y = a\cos\omega t + b\sin\omega t$. Provided a spectrum of frequencies, sine waves are fit by the least-squares method to the data, and the reduced residual sums are plotted against their corresponding frequencies to produce a power spectrum, which is the amount of power each frequency contributes to the data's variance. The equations for the periodogram are given by Barning (1963), Lomb (1976), and Scargle (1982):

$$p(\omega) = \frac{1}{\sum_i y_i^2}\left\{\frac{[\sum_i y_i \cos\omega(t_i-\tau)]^2}{\sum_i y_i \cos^2\omega(t_i-\tau)} + \frac{1}{\sum_i y_i^2}\frac{[\sum_i y_i \sin\omega(t_i-\tau)]^2}{\sum_i y_i \sin^2\omega(t_i-\tau)}\right\} \tag{2.1}$$

where t_i is the time at each measurement, y_i is the value of each measurement, ω is the angular frequency of the sine wave, and τ is given by

$$\tan 2\omega\tau = \frac{\sum_i \sin 2\omega t_i}{\sum_i \cos 2\omega t_i}. \tag{2.2}$$

There are a few drawbacks to this method which must be noted: First, in order for this method of analysis to be valid, the mean of the data must be subtracted ($\bar{y} = 0$). This implies the mean of the fitted sine function is equivalent to the mean of the data, which may not be true, and can be overcome by simply adding a vertical shift, c to the sine function such that $y = a\cos\omega t + b\sin\omega t + c$ (Cumming et al., 1999). Second, the periodogram does not take into account measurement uncertainty. Gilliland and Baliunas (1987) and Irwin et al. (1989) tackle this issue by implementing weighted sums. These alterations to Scargle (1982)'s periodogram made for a more robust analysis in the case of a small number of observations by accounting for potential statistical fluctuations in the mean of the sampled observations and applying appropriate weights to measurements with varying uncertainties.

2.2.1.1 The Generalized Lomb-Scargle (GLS) Periodogram

The periodogram analysis procedure utilized in this work is presented by Zechmeister and Kürster (2009), and is known as the Generalized Lomb-Scargle (GLS) periodogram. The GLS periodogram is the most up-to-date adaptation of the traditional CLS periodogram. The GLS periodogram is acquired the same way as described by Lomb (1976), by fitting a full model sine function, $y(t) = a\cos\omega t + b\sin\omega t + c$, to a time series of N measurements at time t_i and errors σ_i. The function includes an offset, c. For a given grid of frequencies (ω) or periods ($P = \frac{2\pi}{\omega}$), Zechmeister and Kürster (2009) determine the minimum squared difference between the observed data, y_i, and the sine function $y(t)$:

$$\chi^2 = \sum_{i=1}^{N} \frac{[y_i - y(t_i)]^2}{\sigma_i^2}. \tag{2.3}$$

After applying normalized weights ($w_i = \frac{1}{W}\frac{1}{\sigma_i^2}$, where $W = \sum \frac{1}{\sigma_i^2}$, and $\sum w_i = 1$), equation (2.3) becomes

$$\chi^2 = W \sum_{i=1}^{N} w_i [y_i - y(t_i)]^2. \tag{2.4}$$

The periodogram, $p(\omega)$, can be written as the normalized relative χ^2 reduction:

$$p(\omega) = \frac{\chi_o^2 - \chi^2}{\chi_o^2} \tag{2.5}$$

$$p(\omega) = \frac{1}{YY \cdot D}[SS \cdot YC^2 + CC \cdot YS^2 - 2CS \cdot YC \cdot YS] \tag{2.6}$$

where

$$D(\omega) = CC \cdot SS - CS^2 \tag{2.7}$$

and

$$Y = \sum \omega_i y_i \tag{2.8}$$

$$C = \sum \omega_i \cos \omega t_i \tag{2.9}$$

$$S = \sum \omega_i \sin \omega t_i. \tag{2.10}$$

$$YY = \hat{YY} - Y \cdot Y \qquad \hat{YY} = \sum \omega i y_i^2 \tag{2.11}$$

$$YC(\omega) = \hat{YC} - Y \cdot C \qquad \hat{YC} = \sum \omega i y_i \cos \omega t_i \tag{2.12}$$

$$YS(\omega) = \hat{YS} - Y \cdot S \qquad \hat{YS} = \sum \omega i y_i \sin \omega t_i \tag{2.13}$$

$$CC(\omega) = \hat{CC} - C \cdot C \qquad \hat{CC} = \sum \omega i \cos^2 \omega t_i \tag{2.14}$$

$$SS(\omega) = \hat{SS} - S \cdot S \qquad \hat{SS} = \sum \omega i \sin^2 \omega t_i \tag{2.15}$$

$$CS(\omega) = \hat{CS} - C \cdot S \qquad \hat{CS} = \sum \omega i \cos \omega t_i \sin \omega t_i \tag{2.16}$$

The abbreviations with hats on the right-hand column represent the classical sums. The weighted sum of the squared deviations from the weighted mean, ${\chi_o}^2$, is defined as $W \cdot YY$.

Equation (2.5), the generalized Lomb-scargle periodogram, lies within the range $0 \leq p \leq 1$, where $p = 0$ indicates no improvement of the fit and $p = 1$ indicates $\chi^2 = 0$ (in other words, a "perfect" fit). An arbitrary time reference point, τ, can be introduced into the time-dependent sums, which will not affect the χ^2 of the fit ($t_i \rightarrow t_i - \tau$). If τ is chosen as

$$\begin{aligned} \tan 2\omega\tau &= \frac{2CS}{CC - SS} \\ &= \frac{\sum w_i \sin 2\omega t_i - 2 \sum w_i \cos \omega t_i \sum w_i \sin \omega t_i}{\sum w_i \cos 2\omega t_i - [(\sum w_i \cos \omega t_i)^2 - (\sum w_i \sin \omega t_i)^2]} \end{aligned} \tag{2.17}$$

Equation (2.5) becomes

$$p(\omega) = \frac{1}{YY} \left[\frac{YC_\tau^2}{CC_\tau} + \frac{YS_\tau^2}{SS_\tau} \right] \tag{2.18}$$

because the interaction term, CS_τ, disappears and the index, τ, is added to the

time-dependent sums. The difference between Equations (2.1) and (2.18) is that in (2.18) the errors are weighted and there is the second term accounting for the floating mean in Equations (2.14), (2.15), (2.16), and (2.17) (CC_τ, SS_τ, CS_τ, and $\tan 2\omega\tau$, respectively).

2.2.1.2 False Alarm Probability (FAP)

One major challenge when interpreting periodograms arises when noise in the time-series data produces various peaks in the resulting periodogram that are not real. This must be combated by determining the false alarm probability (FAP) for resulting periodogram. The FAP determines the likelihood that at least one of M power values within a prescribed frequency grid computed from a white-noise time-series will equal or exceed a specified value. The greater a signal's power, the less likely it will be flagged as a false alarm. Calculating the FAP can be done analytically and/or by Monte Carlo or bootstrap simulations.

The probability that a specified power can arise purely from noise must first be calculated to determine the FAP. Different periodogram normalization techniques require their own respective probability functions (Table 2.1). The GLS periodogram is normalized to unity, so the probability that at least one other power, p (where $p \in [0, 1]$), will be at or greater than a given value, p_o, is

$$Prob(p > p_o) = (1 - p_o)^{\frac{N-3}{2}}. \tag{2.19}$$

The significance of a peak with power, p_o, compared to peaks at all other sampled frequencies (Zechmeister and Kürster, 2009) is

$$FAP = 1 - [1 - Prob(p > p_o)]^M. \tag{2.20}$$

For a frequency grid with width $\Delta f = f_2 - f_1$ sampled at a resolution $\delta f \approx \frac{1}{T}$ (where

T is the time duration of sampled frequencies), $M = \frac{\Delta f}{\delta f}$. If $f_1 \ll f_2$, then $M \approx T f_2$ (Cumming, 2004). For low FAP values (FAP $\ll 1$) Zechmeister and Kürster (2009) give the approximation,

$$FAP \approx M \ Prob(p > p_o). \tag{2.21}$$

Table 2.1: Probability functions for the likelihood that a periodogram power, p, will be greater than or equal a specified value, p_o (Cumming et al., 1999).

Reference Level	Range	Probability
Population Variance	$p \in [0, \infty)$	$Prob(p > p_o) = \exp(-p_o)$
Sample Variance	$p \in [0, 1]$	$Prob(p > p_o) = (1 - p_o)^{\frac{N-3}{2}}$
Residual Variance	$p \in [0, \infty)$	$Prob(p > p_o) = (1 + \frac{2p_o}{N-3})^{-\frac{N-3}{2}}$

Alternatively, the FAP can be determined by using a Monte Carlo or bootstrap simulation. It must be noted that such numerical techniques require much more time to complete than the computation of the GLS itself. An example of this and how it compares to the analytical procedure is discussed in Section 2.2.1.3.

2.2.1.3 Example Usage on Simulated Data

The GLS procedure can be tested on a simulated data set (Section 3.1.2), modeling the time-series photometric signature of a single star. The rotation period is already known and can be used to test the accuracy of the resulting GLS periodogram. Additionally the reliability of each of the FAP methods can be tested.

The GLS was tested on a model rotation signature with a rotation period of 10 d with an inclination of 90^o and injected gaussian noise. The sampling rate of the "observations" was dictated to be on a nightly basis with intermittent and randomly distributed "weather", that would have inhibited observations of the target. The results of the GLS periodogram analysis successfully picked out a dominant periodic signature of 10 d. The peak corresponding to the period at 10 d returned 0.00%

likelihood that this signal is a false alarm.

2.2.2 Determining Relative Inclination

Using the resulting stellar rotation periods acquired from the time-series photometry (Section 2.1.1) and the $v \sin i$ values extracted from the component resolved spectra (Section 2.1.2), we can disentangle the rotational velocity and inclination from the component $v \sin i$ values using the following relation:

$$\frac{2\pi R_\star}{P_{rot}} \sin i = v \sin i \tag{2.22}$$

where P_{rot} is the equatorial rotation period of the star, $R_\star$ is the radius of the star, and i is the inclination of the star relative to our line of sight. Solving for the inclination, we have:

$$i = \sin^{-1}\left[v \sin i \left(\frac{P_{rot}}{2\pi R_\star}\right)\right] \tag{2.23}$$

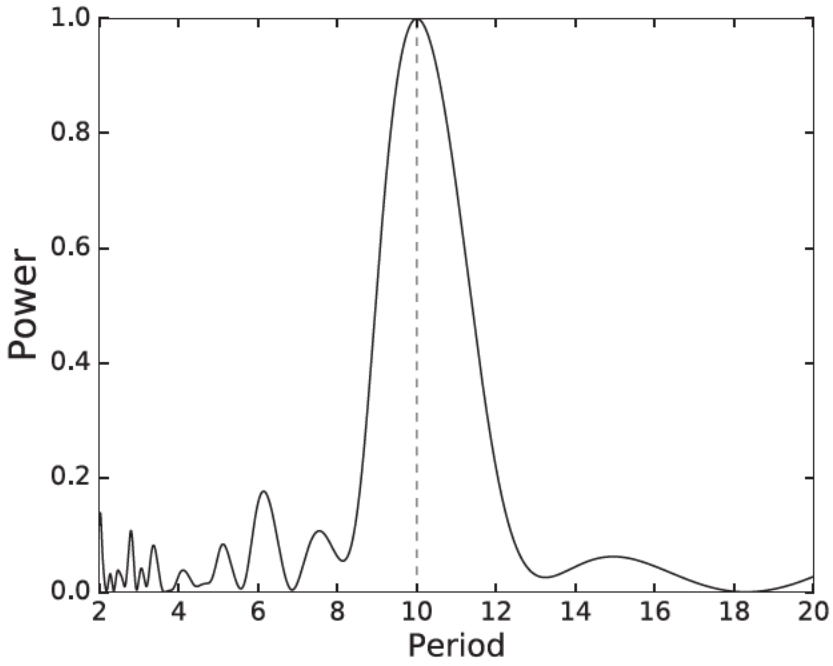

Figure 2.2: The resulting generalized Lomb-Scargle periodogram from a simulation of the observational signature of a single star (see Section3.1.2).

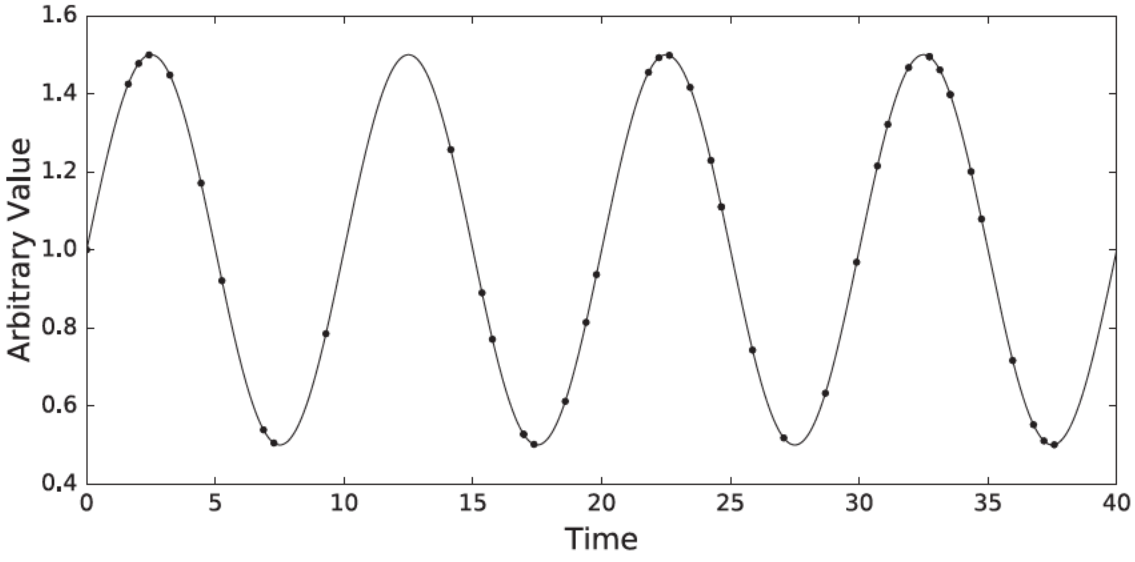

Figure 2.3: A light curve of the model light curve fit to a sinusoid of P = 10 d.

Chapter 3

Modeling Observational Signatures

3.1 Simulating Time-Series Photometry of Unresolved Binary Stars

The purpose of the simulation is to model the time-series photometric signature that would be observed from the presence of star spots on the photospheres of two rotating stars in an unresolved binary system. The code generates the total flux from each star individually and applies scale factors to account for each star's contribution to the total observed flux. Once the individual fluxes are scaled, they are simply added together and injected with Gaussian noise to produce the final "observed" signal. The result generated by the simulation is represented as a normalized flux because the simulation quantifies the change in flux as the ratio of (1) the brightness of the system while it is affected by dimming or brightening to (2) the brightness of the system in the absence of dimming or brightening. The code defines the latter component of this ratio to be 1.0 (effectively normalizing the signal) such that any instances of dimming or brightening can be represented as a contrast ratio, preserving the normalization of the overall signal, and generalizing its usage so that it may be utilized for various physical applications involving flux changes.

3.1.1 User Input

Each star has a set of parameters given as user-definable values:

- minimum and a maximum latitude limits (in degrees) where spots can occur
- minimum and maximum contrast ratios star spots may have
- the star's rotational inclination
- the rotation period in days

The values for spot latitudes and longitudes are generated using a uniform random number generator (latitudes are generated between the specified limits described above and longitudes are between 0 and 360 degrees).
Additional user inputs pertain to the sampling rate of the simulation:

- the total time the model should simulate (in days)
- the sampling time difference (also in days)

And finally, the ratio of the fluxes from each star (flux ratio) is also defined by the user.

3.1.2 Computing the Photometric Signature of Spots on a Single Star

The simulation computes the observed flux of a single star as prescribed by Aigrain et al. (2012), which treats star spots as though they are point-like. Realistically, star spots do have surface area; however, treating the spots as small points is beneficial because it eliminates unnecessary area-dependent calculations while still accomplishing the goal of modeling a spotted star's observational signal. For example, point-like spots obey the assumption that spots never overlap. Additionally, no specific shape

must to be generated for each spot. With no specific shape, spatial projection effects within spots can be ignored. Also, stellar limb-darkening is not taken into account because even though the star's unspotted photospheric brightness decreases toward the limb, so does the brightness of the spot, minimally affecting the spot's photometric signature.

The observed change in flux caused by the kth spot changing its position on the Earthward-facing surface of a single star is

$$F_k(t) = f_k MAX\{\cos\beta_k(t); 0\}^1, \tag{3.1}$$

where t is time, $\beta_k(t)$ is the angle between the spot normal and the line of sight, and f_k represents the difference in flux output the spot would cause if it were located at the center of the stellar disk. f_k is commonly interpreted as a combination of the dimming effects caused by the spot's area and its contrast and can be theoretically determined as follows:

$$f_k = 2(1 - c_k)(1 - \cos\alpha_k), \tag{3.2}$$

where c is the contrast ratio between the spot and the photosphere in the absence of spots, and α_k is the spot's angular radius on the surface of the star. Note there exists a degeneracy between the effects c and α_k have on f_k. To account for the fact we cannot disentangle each parameter's contribution to the observed change in flux, both can effectively be combined into a single term. Thus, we amend Equation 3.2 by dropping the α_k term (because the spots are already mathematically defined to have no area), and f_k becomes

$$f_k = 2(1 - c_k). \tag{3.3}$$

[1] MAX indicates a condition which selects the maximum value of the quantities within the brackets, which is either $cos\beta_k(t)$ or 0.

The $\beta_k(t)$-dependent conditional term in Equation 3.1 applies the projection effect the spot's relative geometric location on the star's surface has on f_k. $\beta_k(t)$ is determined by

$$\cos\beta_k(t) = \cos\phi_k(t)\cos\delta_k\sin i + \sin\delta_k\cos i, \tag{3.4}$$

where δ_k is the latitude of the spot relative to the star's rotational equator, i is the stellar rotational inclination. $\phi_k(t)$ is the phase of the spot relative to the observer's line of sight (the stellar meridian) and is given as

$$\phi_k(t) = \frac{2\pi t}{P_{rot}} + \phi_{k,o}. \tag{3.5}$$

P_{rot} is the star's equatorial rotation period and $\phi_{k,o}$ is the longitude of the spot at $t = 0$. If multiple spots are present on the stellar disk, the total change in observed flux is

$$\Psi(t) = \Psi_o\left[1 - \sum_k^N F_k(t)\right], \tag{3.6}$$

where Ψ_o is the observed flux without the presence of spots ($\Psi_o = 1$), and N is the total number of spots.

3.1.3 Application to an Unresolved Binary System

The method described above can be used to simulate the total observed flux from two stars in an unresolved binary system. First, the each flux is calculated individually for both components. At this stage in the simulation the normalized flux outputs are not yet combined, so the fluxes of the primary and secondary (F_p and F_s, respectively) both equal 1 in the absence of spots, representing the system as though it is component-resolved. However, the normalized flux from the system must represent *unresolved* observations, requiring that sum of each components' contributing flux equals 1. Thus, each star's flux output must be scaled such that for a spotless

photosphere,

$$s_p F_p + s_s F_s = 1 \tag{3.7}$$

where s_p and s_s are the scale factors for the primary and secondary components, respectively. Because F_p and F_s equal 1, Equation 3.8 reduces to

$$s_p + s_s = 1. \tag{3.8}$$

Additionally, the ratio of the scale factors is equivalent to the empirical flux ratio of the primary and secondary components of the binary system being modeled ($\mathcal{F}_{ratio}$), and can be written as

$$\mathcal{F}_{ratio} = \frac{s_p}{s_s}. \tag{3.9}$$

Equations (3.8) and (3.9) share properties which can be used in a system of equations to determine the value of each scale factor. Rearranging (3.9) for s_s, then substituting into (3.8) results in the following calculation to obtain s_p:

$$s_p = \left[1 + \frac{1}{\mathcal{F}_{ratio}}\right]^{-1} \tag{3.10}$$

and subsequently, s_s:

$$s_s = 1 - s_p. \tag{3.11}$$

The scaling factors are then applied to the flux output of their respective stellar component at each time step in its rotation (for a spotted photosphere, F_p and $F_s \leq 1$). The resulting sum of the scaled fluxes is a correctly normalized model of the photometric signature created by spots on the surface of two unresolved rotating stars.

Chapter 4

Case Study: DF Tau

4.1 Overview

DF Tau is a young (∼1.5 Myr) visual binary in the Taurus star-forming region (Herbig and Bell, 1988) with an angular separation of ∼100 mas, corresponding to 14 AU given the distance to Taurus of ∼140 pc (Kenyon et al., 1994). Interestingly, only one component shows evidence (Figure 4.1) of having a circumstellar disk even though both stars are coeval – a situation not dissimilar to the results (Figure 1.4) presented by Karim et al. (2016), with the exception that DF Tau possesses the advantages of belonging to a multiple star system. DF Tau is thus a key component in the investigation of PMS disk evolution because its properties can help inform disk-dissipation processes that do not assume WTTS are a product of CTTS.

Table 4.1: Component Properties

Property	Primary	Secondary	Ref.
Spectral Type	M2	M2	Allen et al. (2017)
V Magnitude	12.43±0.06	13.10±0.1	White and Ghez (2001)
$v \sin i$	13±4	41±4	Allen et al. (2017)
veiling	0.6±0.1	0.0±0.1	Allen et al. (2017)

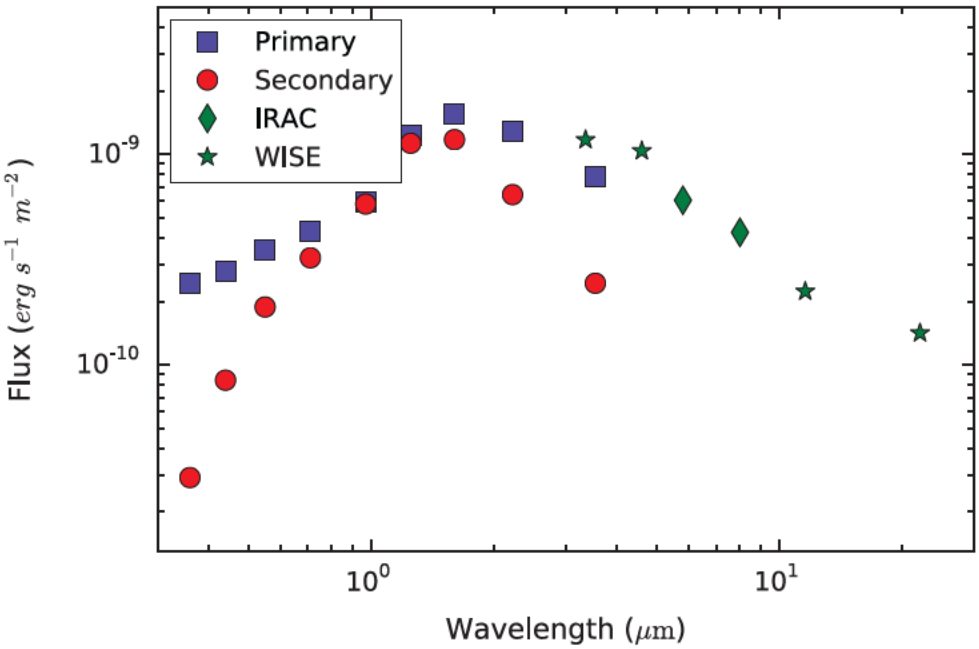

Figure 4.1: Spectral energy distributions of DF Tau's components indicate that the primary has excess flux in the UV and NIR, which is a strong indication it has a circumstellar disk. The secondary component does not, and is therefore unlikely to have a disk. In this figure presented by Allen et al. (2017), the blue squares represent de-reddened visible photometry of the primary component, red circles are NIR photometry of the secondary, green diamonds correspond to unresolved photometry at the [5.8] and [8.0] Spitzer bands, and the green stars represent unresolved WISE photometry.

4.2 Analysis

All photometry acquired of DF Tau to date were analyzed as a single unit (Figure 4.2) and on a single-epoch basis. A GLS analysis set to probe periodic signals from 2 to 12,000 days was performed on the entire set of V-band archival photometry, which revealed a strong signal of ∼20 years (Figure 4.3) for the primary component. Interestingly, this signal is half of the orbital period of the DF Tau binary components (Schaefer et al., 2014; Allen et al., 2017), which may suggest stellar activity cycles may be affected by the orbit of the secondary component, although this is unlikely. A second analysis probing the short-period range (2 - 20 days) revealed a strong peak in the resulting periodogram at ∼10.4 d and is likely to represent the rotation period

of the primary component throughout the decades-long observational record because the primary component is ∼3 times brighter than the secondary in the V-band.

A single-epoch GLS analysis of photometry acquired with the Lowell Observatory 31 inch Telescope (Figures4.4, 4.5) reveals the primary component's rotation period to be ∼10.5 d, which is consistent within 1/10 of a day of the rotation period recovered from DF Tau's the entire photometric history. Under the assumption the secondary component's rotation period is the next strongest signal output from the system, this implies the rotation period of the secondary to be ∼9.3 d. We will analyze this assumption in Section 4.2.2.

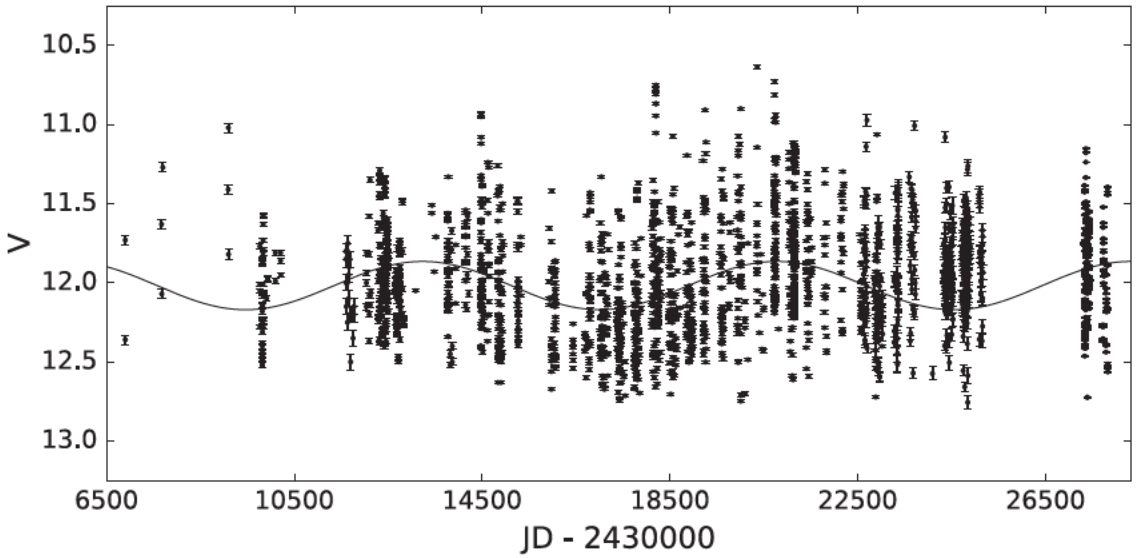

Figure 4.2: Light curve of the entire archival collection of DF Tau photometry in the V band (Varsavsky, 1961; Smak, 1964; Mendoza, 1967; Petrov, 1976; Zaitseva and Liutyi, 1976; Shevchenko and Shutyomova, 1981; Rydgren et al., 1984; Shajmieva and Shutemova, 1985; Bouvier et al., 1986, 1993, 1995; Pojmanski, 2005; Shakhovskoj et al., 2006; Grankin et al., 2007; Allen et al., 2017). A sinusoidal fit with a period of 20.49 years is plotted over the data set.

4.2.1 Component Parameters

Although DF Tau is a thoroughly studied object, reliably determined component masses have not been determined until recent years (Schaefer et al., 2012; Allen

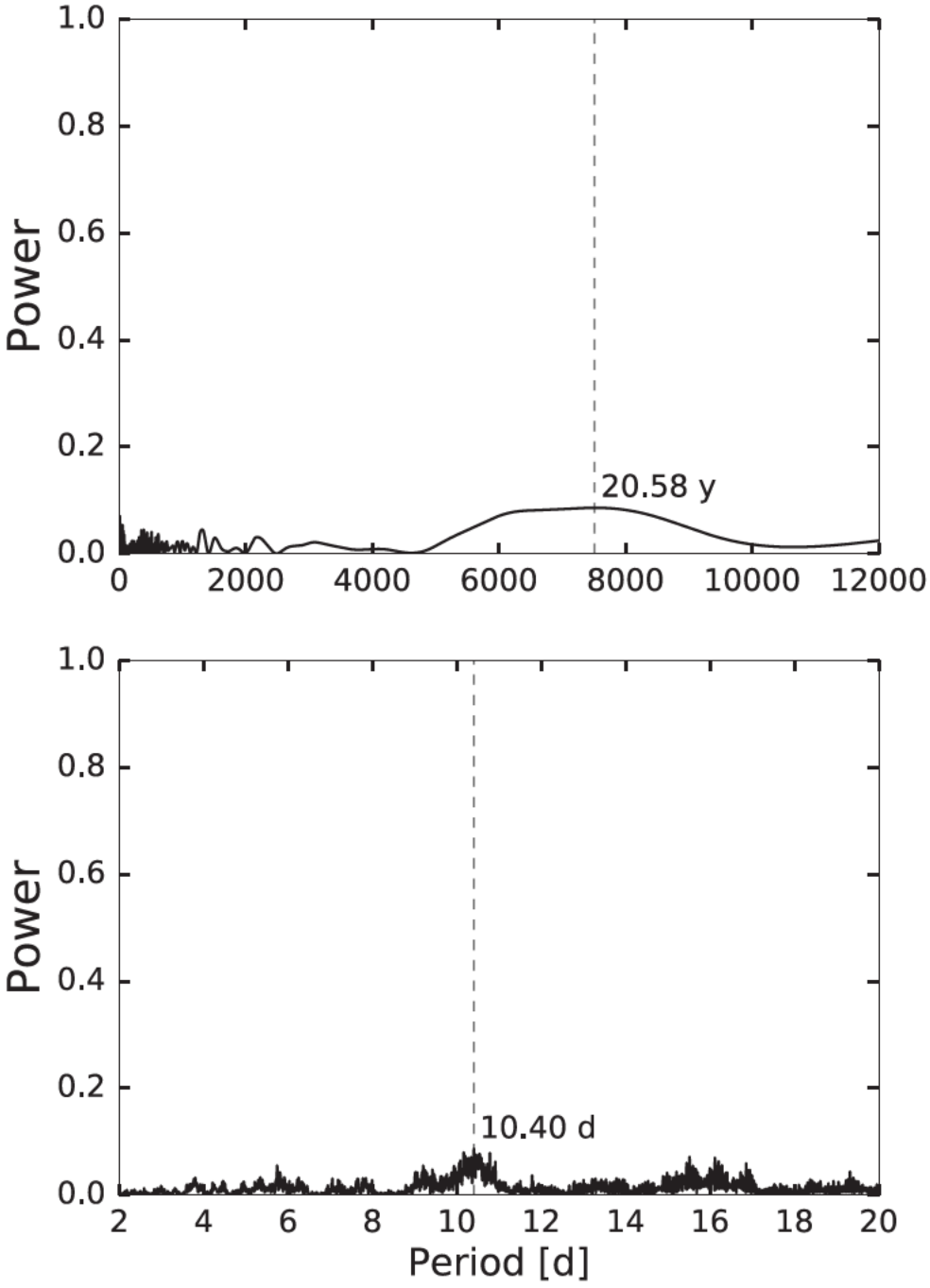

Figure 4.3: *Top*: Lomb-Scargle periodogram analysis of entire archival collection of DF Tau photometry in the V band indicating the primary component's long term activity cycle is ∼20 years and has a FAP of 0.00 (within the precision) for all MC and analytic techniques. *Bottom*: Short-period periodogram analysis for all archival data indicating a primary rotation period of 10.4 d.

et al., 2017), and there has been considerable variation in reported radii (Table 4.2). Prior to this work, the most up-to-date masses and radii of both DF Tau's primary and secondary components are 0.59±0.15 $M_\odot$ and 2.1 $R_\odot$, and the only component-resolved determinations of $v \sin i$ are 13±4 km s^{-1} and 41±4 km s^{-1}, respectively (Allen et al., 2017).

The inclination of DF Tau's primary stellar component can be found using Equation 2.23. However, an initial calculation using the input parameters P = 10.5 d, $R_\star$ = 2.1 $R_\odot$, and $v \sin i$ = 13±4 km s^{-1} returns an unreal result (i.e., the inverse sin of a term greater than 1 does not return a physically possible value). This suggests the stellar radius is likely underestimated. Closer investigation of $R_\star$ approximates a lower limit of 2.7±0.84 $R_\odot$ (when i = 90 degrees), which is consistent with the radius of a 1.5 Myr old, 0.6 $M_\odot$ star as predicted using model isochrones by Baraffe et al. (2015). We adopt this radius for both stellar components; thus the rotation inclination of the primary is determined to be 90 degrees relative to the line of sight of the observer.

Determining the secondary's rotation inclination using the input parameters P = 9.3 d, $R_\star$ = 2.7 $R_\odot$, and $v \sin i$ = 41±4 km s^{-1} presented a similar issue, producing a non-real result. This indicates the 9.3 d periodic signal identified by the periodogram analysis does not correspond to the rotation period of the secondary. An upper limit can be estimated assuming i = 90 degrees, which gives $P \leq$ 3.3 d. This is consistent with the much larger value of $v \sin i$ for the secondary star, indicating more rapid rotation. The large discrepancy in rotation periods is also consistent with the observation that a disk only exists around the primary because a larger rotation period signifies its rotation is likely regulated by disk-locking, whereas the smaller rotation period of the secondary suggests it is not subject to disk-locking.

Table 4.2: Previously published properties

$\frac{M_\star}{M_\odot}$	P_{rot} [d]	$\frac{R_\star}{R_\odot}$	$v \sin i$ [km s^{-1}]	i [deg]	Ref.
...	...	...	<35	...	Vogel and Kuhi (1981)
...	>10	...	...	...	Rydgren et al. (1984)
...	...	...	21.6±9.2	...	Bouvier et al. (1986)
0.8	...	3.8	...	...	Bertout et al. (1988)
...	8.5	...	...	65±25	Bouvier and Bertout (1989)
...	...	...	19.7±7.8[a] 16.1±5.3[b]	...	Hartmann and Stauffer (1989)
...	...	...	20	...	Basri and Batalha (1990)
...	7.9	...	...	...	Richter et al. (1992)
...	...	...	18±4	...	Bertout et al. (1993)
...	8.5	3.0	16.1±5.3	64	Bouvier et al. (1995)
0.17	...	3.9	...	...	Hartigan et al. (1995)
...	7.3±0.4[c]	...	...	...	Johns and Basri (1995)
...	7.0±0.2[d]	...	21.7±5.3	...	Johns-Krull and Basri (1997)
0.27	...	3.37	...	...	Gullbring et al. (1998)
...	7.2±0.3	...	...	...	Chelli et al. (1999)
...	...	...	...	85	Johns-Krull and Valenti (2001)
0.39	7.18	3.55	...	52	Artemenko et al. (2012)
0.59±0.15	10.55	2.1	13±4$_p$ 41±4$_s$	...	Allen et al. (2017)

[a] Kitt Peak National Observatory 4 m Telescope
[b] Fred L. Whipple Observatory 1.5m
[c] Variability found in Hα
[d] Variability found in He I 5876 $\mathring{A}$

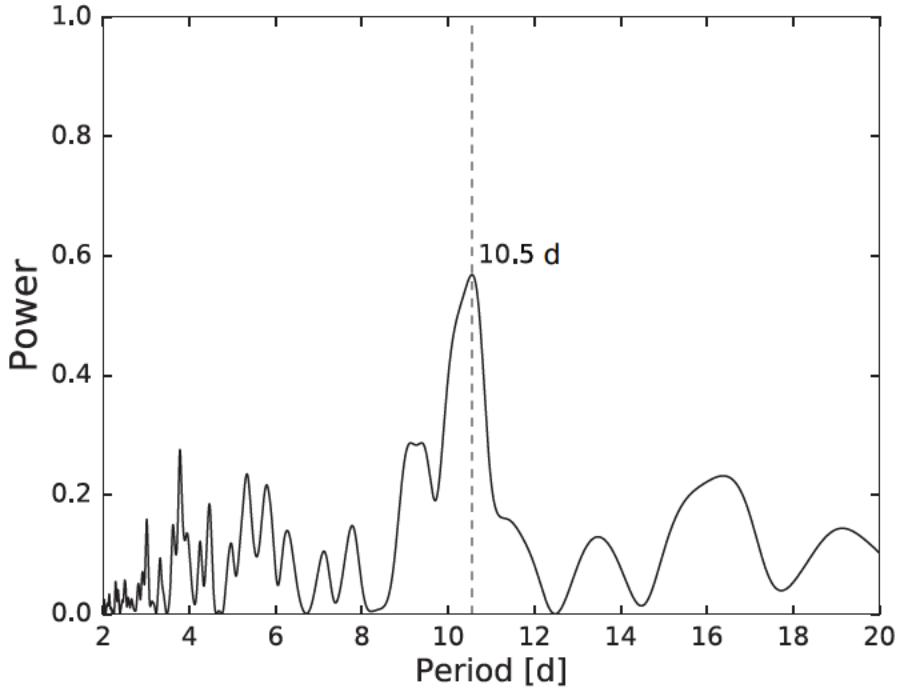

Figure 4.4: Lomb-Scargle periodogram analysis of V band photometry acquired with the Lowell Observatory 31 inch telescope. The maximum detected signal of 10.5 d is consistent with Allen et al. (2017) and has a FAP of 0.00 within the precision for all MC and analytic techniques.

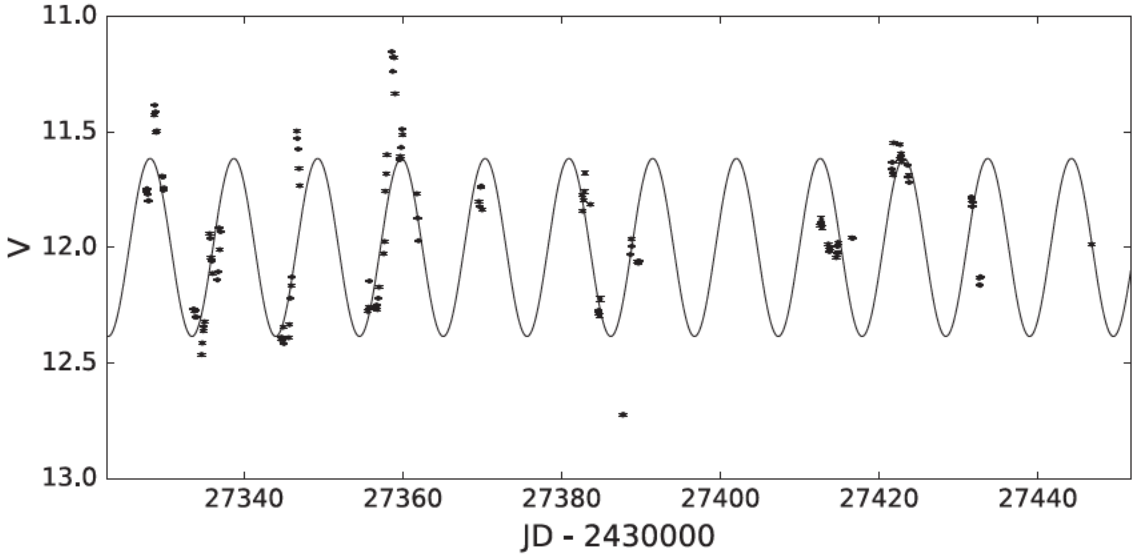

Figure 4.5: V-band, time-series photometry of DF Tau taken with the Lowell 31-inch telescope.

4.2.2 Accretion-driven Periodicity?

The 9.3 d periodic signal is likely not generated by the secondary component's rotation period, it is also probably not a false signal resulting from the irregular sampling (Allen et al., 2017). We cannot rule out that the source of the signal has a physical explanation.

It is possible the source of this signal originates from hot spots resulting from magnetospheric accretion onto the primary star (Ghosh and Lamb, 1978). Lamb et al. (1985) suggest that material accretes onto an inclined magnetosphere where the magnetic field appears stronger The signature is pronounced at specific phases in relation to $\omega_K(r)$ and $\omega_\star$, where $\omega_K(r)$ is the angular frequency associated with the Keplarian orbital velocity of the clump of accreting material, and $\omega_\star$ is that of the magnetospheric rotation (also the rotation period of a disk-locked star). Bouvier and Bertout (1989) speculate that CTTS can exhibit similar behavior resulting from an inclined magnetospheric structure that could cause a shift in the period when interacting with accreting inner-disk material of a non-uniform density. The observed change in the phase of the brightness signature caused by hot spots relative to the rotation of the star is

$$\Delta Phase = \frac{2\pi}{\omega_K(r) - \omega_\star}. \tag{4.1}$$

In a state of rotational equilibrium, hot spots' longitude remains mostly stationary, so no rotational phase offset is likely to be observed (Bouvier et al., 2007). If the rate of accretion increases as a result of more clumpy inhomogeneities in the inner disk, then the hot spots' angular velocity at the base of the stream also increases and changes its position by a small amount. The stars with misaligned magnetospheres tend to accrete matter streams and can be known to spiral along the magnetic equator (Bouvier et al., 2007). The resulting variability of a star with hot spots typically causes 1-2 peaks in brightness per period, depending on β, the angle between the

star's rotation axis and the magnetic dipole moment, and ϕ, the inclination of the dipole to the observer.

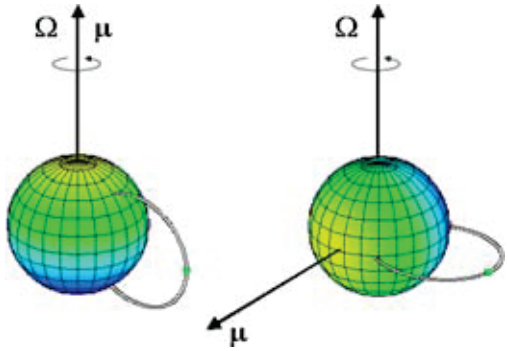

Figure 4.6: Geometry of an aligned and inclined magnetospheric dipole (Gregory et al., 2006). *Left*: An aligned dipole with the dipole moment μ aligned with the stellar rotation axis, Ω. *Right*: A misaligned dipole with an inclination of 90 degrees relative the the star's rotation axis.

Alternatively, magnetic dynamo and accretion models by von Rekowski and Piskunov (2006) show that accretion causes the star to spin-up at latitudes where material meets the star. Analysis of hotspot distribution on T Tauri stars in relation to magnetospheric inclination (Figure 4.6) (Gregory et al., 2006) agrees with Bouvier et al. (2007), showing that along inclined magnetic dipoles ($\beta > 0$), accretion typically falls onto lower latitudes compared to aligned dipolar fields ($\beta = 0$) (Figure 4.7). In the inclined case, where matter accretes onto equatorial regions of the star, there is a significant positive net torque along a thin strip around the same latitudinal region of the stellar surface. In addition, dipolar accretion models of DF Tau in particular (Gregory et al., 2006) show that greater-inclined magnetic fields exhibit increased accretion rates. This would likely strengthen the effect of positive torque along lower latitudes, yielding a greater phase offset than seen with aligned dipoles.

Light curve models of the unresolved photometric variability of the system are used investigate whether the 9.3 day signal corresponds to a phase-offset caused by accreting material. The model follows the prescription of Aigrain et al. (2012) to simulate the time-series photometric signature observed as an effect of the presence

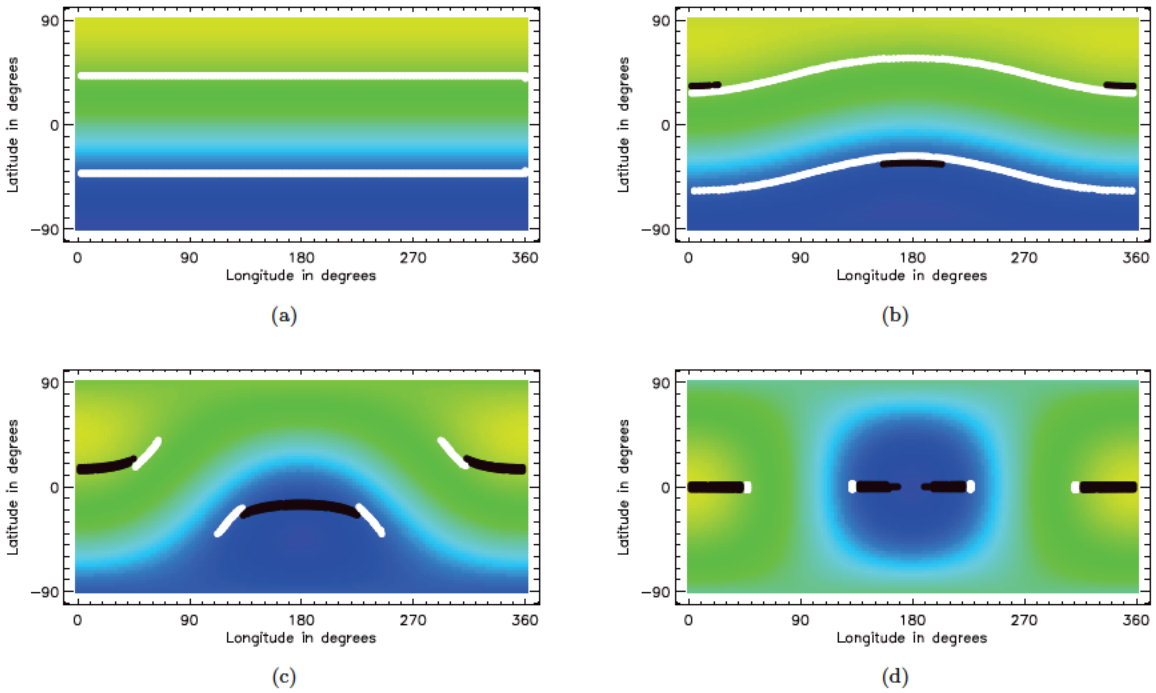

Figure 4.7: Field line footprints along stars with various magnetic inclinations (Gregory et al., 2006). White points represent closed accreting field lines, and black points indicate open accreting field lines. *(a)*: An aligned dipole. $\beta = \mu$ - $\Omega = 0$. *(b)*: An inclined dipole with $\beta = 15$ degrees. *(c)*: $\beta = 45$ degrees. *(d)*: $\beta = 90$ degrees.

of star spots on the stellar photospheres of an unresolved binary system (Section 3). The photometric variability of each component is determined from the FGS data shown in Figure 4.8. The primary component rotation period was set to 10.5 d, and we set the secondary rotation period to 3.14 d. The cool spots are generated via a random uniform distribution between 10 and 70 degrees latitude and 0 to 360 degrees longitude for each star.

Procedural modifications were implemented to test accretion signals by incorporating hot spots into the already randomly generated values for spot contrast. Hot spots that are ∼1% brighter than the photospheric surface produce relative brightness changes that follow closely to typical filling factors between 2 and 4% (Gregory et al., 2006; Valenti and Johns-Krull, 2004). Latitudes where hot spots can occur are limited according to a given β (Gregory et al., 2006). Assuming the clumps of accreting material originate from the corotation radius, R_{CO} of ∼0.06 AU (6.14 $R_\star$)

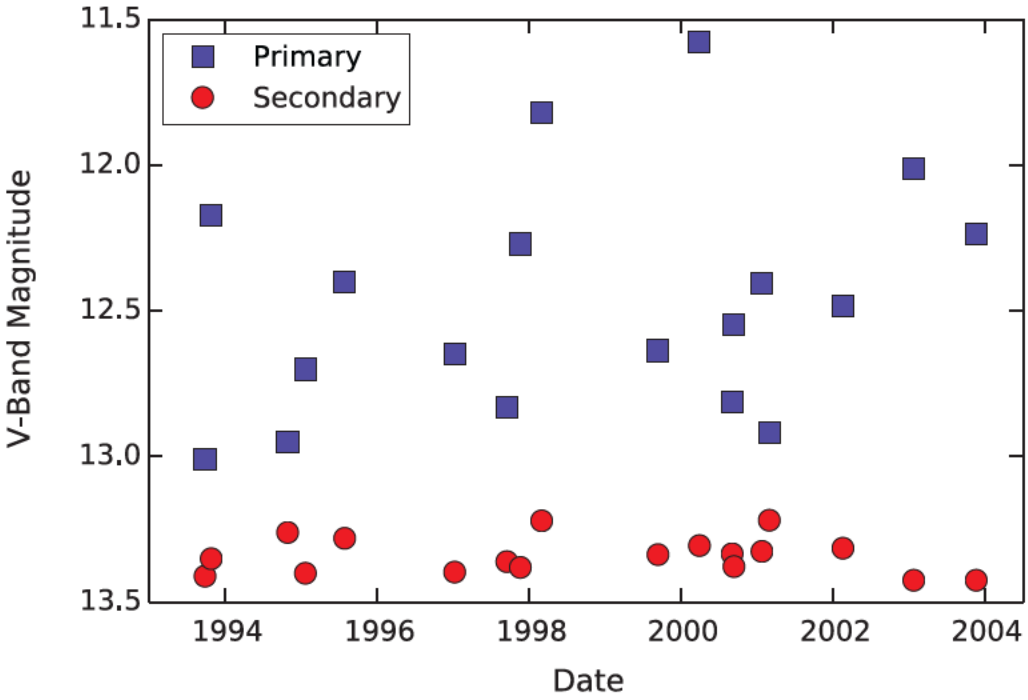

Figure 4.8: Hubble Space Telescope Fine Guidance Sensor V-band photometry of DF Tau from Schaefer et al. (2003, 2006). The primary component of the system is represented by the blue squares, and the secondary component is represented by the red circles. The secondary appears fainter in the V-band and has less peak-to-peak photometric variability (∼0.2 mag) than the primary (∼1.4 mag).

(France et al., 2012), we can predict the change in angular velocity of the material such that the longitudinal phase of the hot spots increases by 3 degrees per time step. Figures 4.9, 4.10, and 4.11 provide visualizations of various steps of the simulation as an example showing what a single iteration out of 10,000 iterations of the code might look like.

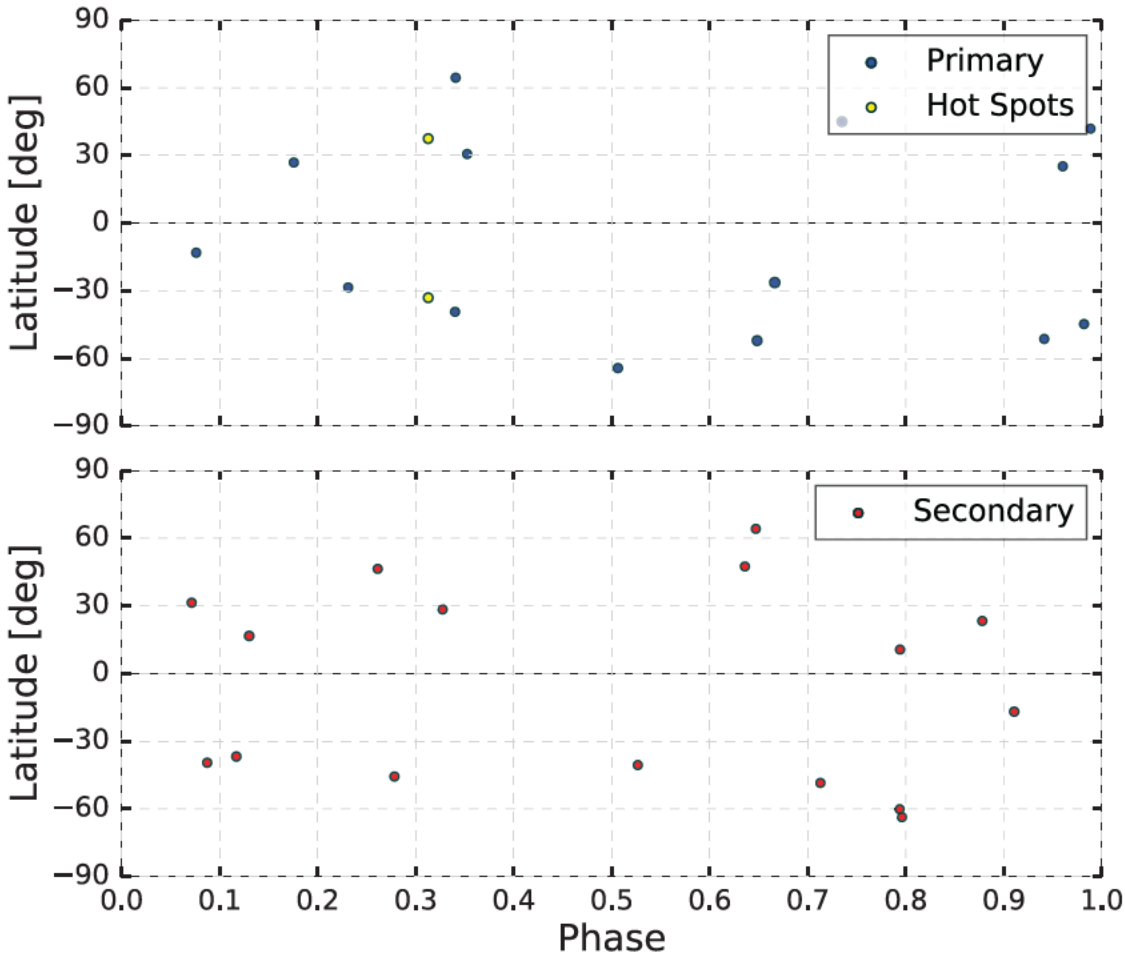

Figure 4.9: Spot maps of the primary and secondary components of the example binary V-band simulation generated to resemble DF Tau (Figure 4.10). Cool spots are represented by blue and red circles for the primary and secondary components, respectively, and yellow circles are accretion-driven hot spots present only on the primary. Spot properties such as latitude, phase, and contrast are determined randomly within a limited-range uniform distribution.

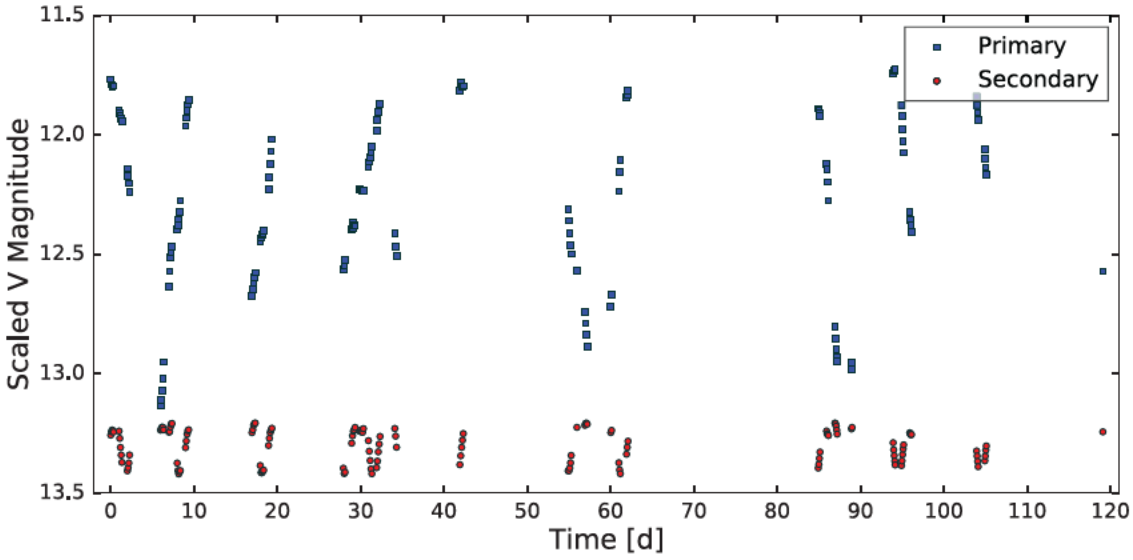

Figure 4.10: Example V-band light curve simulation of a component-resolved binary system with the same observing cadence as observations acquired by Allen et al. (2017). The primary component of the system is represented by blue squares, and the secondary component is represented by red circles. Both components are plotted prior to the injection of Gaussian noise. Input parameters were chosen to closely resemble the individual magnitude variations of the individual components of DF Tau observed by Schaefer et al. (2003, 2006) (Figure 4.8) as well as the periods and inclinations derived from the analysis presented in this work.

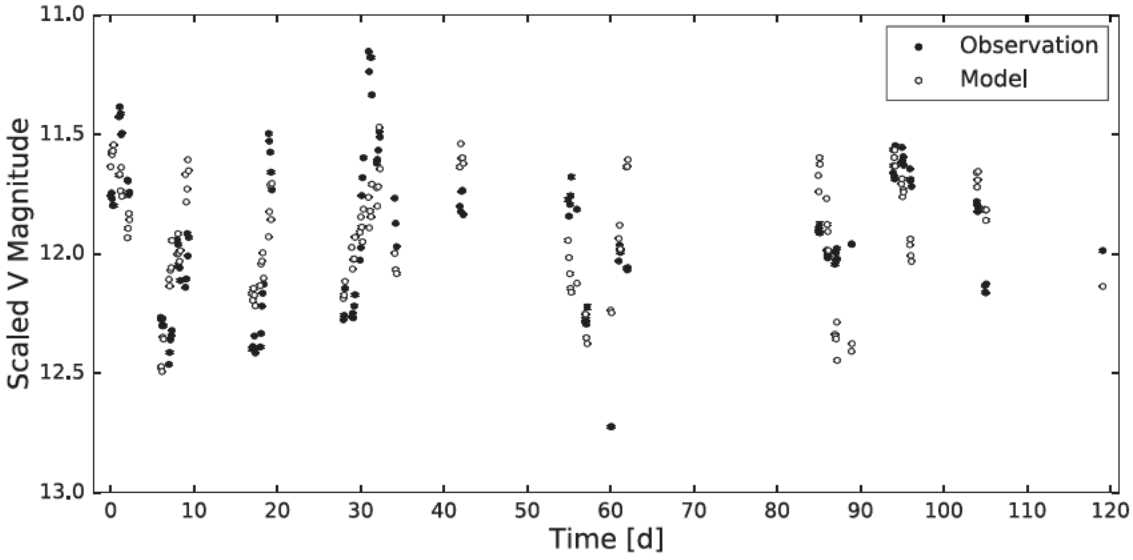

Figure 4.11: The same binary simulation displayed in Figure 4.10, now unresolved, injected with Gaussian noise, and scaled to the mean V-band magnitude of the unresolved DF Tau system (Allen et al., 2017). Model observations are represented by open circles, and observed time-series data are plotted as filled circles for comparison.

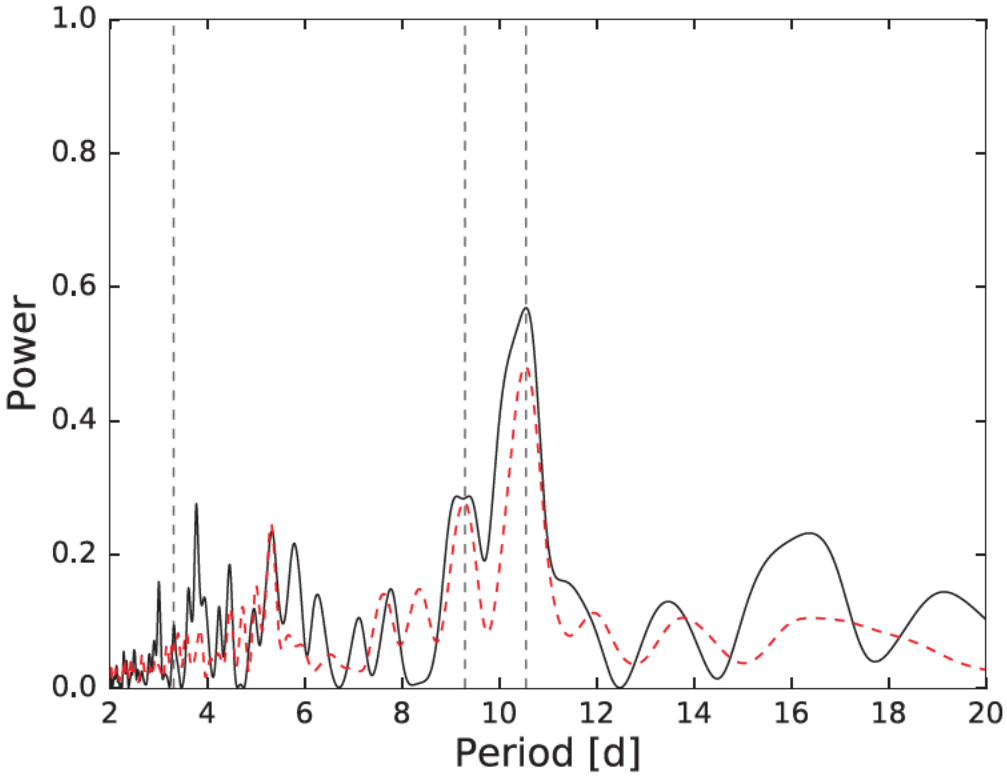

Figure 4.12: Resulting power spectrum averaged over all ten thousand light curve iterations generated in the model simulation.

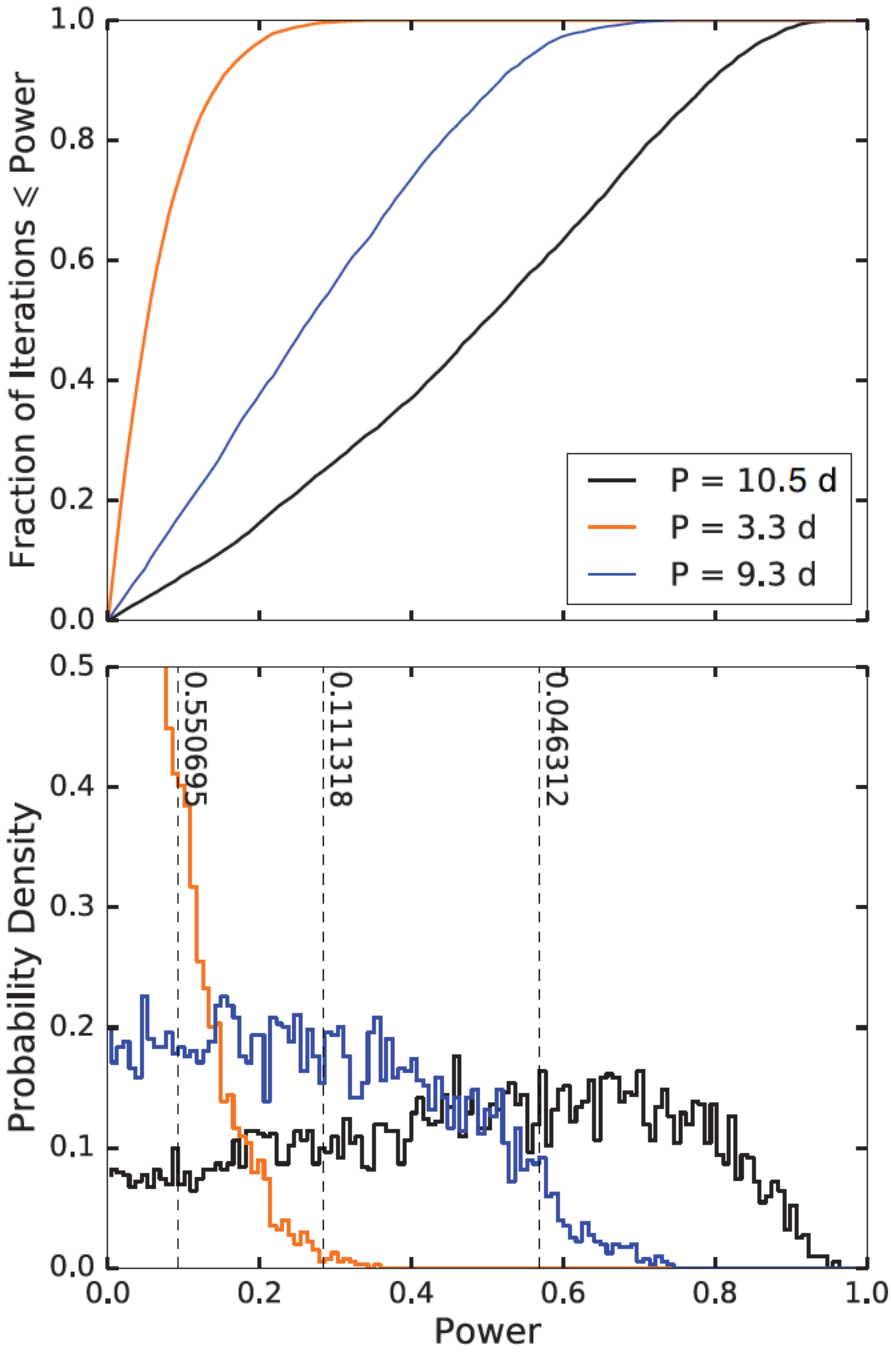

Figure 4.13: *Top*: Cumulative distribution of power signal strengths for 10.5, 9.3, and 3.3 d. *Bottom*: Probability density distributions corresponding to cumulative distributions for the respective periods. Vertical dashed lines indicate the associated FAP for periods at 10.5, 9.3, and 3.3 d from right to left, respectively.

Chapter 5

Conclusions and Future Work

The rotation period of the primary stellar component of the young binary DF Tau was extracted using a Generalized Lomb-Scargle periodogram analysis from unresolved V-band time-series photometry acquired at the Lowell Observatory 31 inch Telescope. NIR spectra obtained with Keck/NIRSPEC provided $v \sin i$ measurements for both the primary and secondary components of the system (Allen et al., 2017). The inclination of the primary component's rotation axis was determined using photometric the rotation period (10.5 d with FAP = 0.00) and corresponding $v \sin i$ (13$\pm$4 km s^{-1}), and is vertical with respect to the line of sight of the observer. The Lomb-Scargle periodogram analysis produced a second strong signal at 9.3 d, however it is unlikely this is the rotation period of the secondary component because an estimate of the upper limit ($i = 90$ degrees, $v \sin i = 41\pm4$ km s^{-1}) yielded a maximum rotation period of 3.3 d. This demonstrates the primary is rotating slower than the secondary, providing further evidence in support of primary having a disk that is regulating its rotation velocity, whereas the secondary does not. Additionally, the rotation inclinations of both stars are nearly perpendicular to the line of sight, therefore indicating a misalignment between the stars' rotation axes and the orbital plane by $\sim$54 degrees. This also suggests the plane of the disk is also misaligned with respect to the orbital

plane.

Ten thousand model light curve simulations were generated for a binary system given the same photometric flux ratio, observing cadence, rotation periods, and component rotation inclinations as acquired with the photometric and spectroscopic analysis of DF Tau summarized above. All model light curves were subject to a Lomb-Scargle analysis and all results were averaged to produce a single statistically representative power spectrum. The model power spectrum was compared against the original produced from the real photometry. The 10.5 d periodic signal was reproduced by the model, however the 3.3 d period did not produce a signal that could be reliably extracted from the power spectrum. The absence of the secondary rotation period indicates it is also not recoverable from the observed light curve. The 9.3 d signal was also absent, suggesting its appearance in the observed power spectrum is not a result of the time-sampling variation between observations. The strong periodic signal at 9.3 d may originate from accretion-induced hot spots on the surface of the primary component. Photospheric hot spots exhibit an apparent shift in rotation frequency relative to cool spots depending on the distance between the stellar surface and the inner disk radius. The simulation was amended to account for the presence of hot spots provided DF Tau's known corotation radius. The same iterative procedure produced an averaged power spectrum displaying a 9.3 d signal of similar strength as seen in the analysis of the observed light curve.

There is no indiction the relative inclination of DF Tau's primary and secondary rotation axes is probable cause for neither prolonged nor premature disk lifetimes. Provided both stars are coeval and possess the same mass and radius, the most likely explanation is that not all disks form with the same properties. For example, it is possible young stars may not emerge from the protostellar stage with disks at all, and may also not be a symptom of binarity. These conclusions imply the necessity of a statistically-fashioned analysis of the remaining young binaries in our sample.

Bibliography

S. Aigrain, F. Pont, and S. Zucker. A simple method to estimate radial velocity variations due to stellar activity using photometry. , 419:3147–3158, Feb. 2012. doi: 10.1111/j.1365-2966.2011.19960.x.

T. Allen, L. Prato, N. Wright-Garba, G. Schaefer, L. I. Biddle, B. Skiff, I. Avilez, R. Muzzio, and M. Simon. Properties of the Closest Young Binaries I: DF Tau's Unequal Circumstellar Disk Evolution. , 2017.

S. A. Artemenko, K. N. Grankin, and P. P. Petrov. Rotation effects in classical T Tauri stars. *Astronomy Letters*, 38:783–792, Dec. 2012. doi: 10.1134/S1063773712110011.

P. Artymowicz and S. H. Lubow. Dynamics of binary-disk interaction. 1: Resonances and disk gap sizes. , 421:651–667, Feb. 1994. doi: 10.1086/173679.

I. Baraffe, D. Homeier, F. Allard, and G. Chabrier. New evolutionary models for pre-main sequence and main sequence low-mass stars down to the hydrogen-burning limit. , 577:A42, May 2015. doi: 10.1051/0004-6361/201425481.

F. J. M. Barning. The numerical analysis of the light-curve of 12 Lacertae. , 17:22, Aug. 1963.

G. Basri and C. Batalha. Hamilton echelle spectra of young stars. I - Optical veiling. , 363:654–669, Nov. 1990. doi: 10.1086/169374.

C. Bertout, G. Basri, and J. Bouvier. Accretion disks around T Tauri stars. , 330: 350–373, July 1988. doi: 10.1086/166476.

C. Bertout, J. Bouvier, W. J. Duschl, and W. M. Tscharnuter. Accretion Disks around T-Tauri Stars - Part Four - the Disk-Star Boundary Layer. , 275:236, Aug. 1993.

J. Bouvier and C. Bertout. Spots on T Tauri stars. , 211:99–114, Feb. 1989.

J. Bouvier, C. Bertout, W. Benz, and M. Mayor. Rotation in T Tauri stars. I - Observations and immediate analysis. , 165:110–119, Sept. 1986.

J. Bouvier, S. Cabrit, M. Fernandez, E. L. Martin, and J. M. Matthews. Coyotes-I - the Photometric Variability and Rotational Evolution of T-Tauri Stars. , 272:176, May 1993.

J. Bouvier, E. Covino, O. Kovo, E. L. Martin, J. M. Matthews, L. Terranegra, and S. C. Beck. COYOTES II: SPOT properties and the origin of photometric period variations in T Tauri stars. , 299:89, July 1995.

J. Bouvier, S. H. P. Alencar, T. J. Harries, C. M. Johns-Krull, and M. M. Romanova. Magnetospheric Accretion in Classical T Tauri Stars. *Protostars and Planets V*, pages 479–494, 2007.

P. W. Cauley, C. M. Johns-Krull, C. M. Hamilton, and K. Lockhart. Testing Disk-locking in NGC 2264. , 756:68, Sept. 2012. doi: 10.1088/0004-637X/756/1/68.

A. Chelli, L. Carrasco, R. Mújica, E. Recillas, and J. Bouvier. Periodic changes of veiling and circumstellar grey extinction in DF Tauri. I. Dust clouds spiraling into a T Tauri star? , 345:L9–L13, May 1999.

L. A. Cieza, D. L. Padgett, L. E. Allen, C. E. McCabe, T. Y. Brooke, S. J. Carey, N. L. Chapman, M. Fukagawa, T. L. Huard, A. Noriga-Crespo, D. E. Peterson, and L. M. Rebull. Primordial Circumstellar Disks in Binary Systems: Evidence for Reduced Lifetimes. , 696:L84–L88, May 2009. doi: 10.1088/0004-637X/696/1/L84.

A. Cumming. Detectability of extrasolar planets in radial velocity surveys. , 354: 1165–1176, Nov. 2004. doi: 10.1111/j.1365-2966.2004.08275.x.

A. Cumming, G. W. Marcy, and R. P. Butler. The Lick Planet Search: Detectability and Mass Thresholds. , 526:890–915, Dec. 1999. doi: 10.1086/308020.

T. F. Droege, M. W. Richmond, M. P. Sallman, and R. P. Creager. TASS Mark IV Photometric Survey of the Northern Sky. , 118:1666–1678, Dec. 2006. doi: 10.1086/510197.

K. France, E. Schindhelm, G. J. Herczeg, A. Brown, H. Abgrall, R. D. Alexander, E. A. Bergin, J. M. Brown, J. L. Linsky, E. Roueff, and H. Yang. A Hubble Space Telescope Survey of H_2 Emission in the Circumstellar Environments of Young Stars. , 756:171, Sept. 2012. doi: 10.1088/0004-637X/756/2/171.

P. Ghosh and F. K. Lamb. Disk accretion by magnetic neutron stars. , 223:L83–L87, July 1978. doi: 10.1086/182734.

R. L. Gilliland and S. L. Baliunas. Objective characterization of stellar activity cycles. I - Methods and solar cycle analyses. , 314:766–781, Mar. 1987. doi: 10.1086/165103.

K. N. Grankin, S. Y. Melnikov, J. Bouvier, W. Herbst, and V. S. Shevchenko. Results of the ROTOR-program. I. The long-term photometric variability of classical T Tauri stars. , 461:183–195, Jan. 2007. doi: 10.1051/0004-6361:20065489.

K. N. Grankin, J. Bouvier, W. Herbst, and S. Y. Melnikov. Results of the ROTOR-program. II. The long-term photometric variability of weak-line T Tauri stars. , 479:827–843, Mar. 2008. doi: 10.1051/0004-6361:20078476.

S. G. Gregory, M. Jardine, I. Simpson, and J.-F. Donati. Mass accretion on to T Tauri stars. , 371:999–1013, Sept. 2006. doi: 10.1111/j.1365-2966.2006.10734.x.

E. Gullbring, L. Hartmann, C. Briceño, and N. Calvet. Disk Accretion Rates for T Tauri Stars. , 492:323–341, Jan. 1998. doi: 10.1086/305032.

P. Hartigan, S. Edwards, and L. Ghandour. Disk Accretion and Mass Loss from Young Stars. , 452:736, Oct. 1995. doi: 10.1086/176344.

L. Hartmann and J. R. Stauffer. Additional measurements of pre-main-sequence stellar rotation. , 97:873–880, Mar. 1989. doi: 10.1086/115033.

A. Henden. New Release of the BSM Epoch Photometry Database. *Journal of the American Association of Variable Star Observers (JAAVSO)*, 44:84, June 2016.

G. H. Herbig and K. R. Bell. *Third Catalog of Emission-Line Stars of the Orion Population : 3 : 1988*. 1988.

W. Herbst, J. Eislöffel, R. Mundt, and A. Scholz. The Rotation of Young Low-Mass Stars and Brown Dwarfs. *Protostars and Planets V*, pages 297–311, 2007.

J. Hernández, L. Hartmann, T. Megeath, R. Gutermuth, J. Muzerolle, N. Calvet, A. K. Vivas, C. Briceño, L. Allen, J. Stauffer, E. Young, and G. Fazio. A Spitzer Space Telescope Study of Disks in the Young σ Orionis Cluster. , 662:1067–1081, June 2007. doi: 10.1086/513735.

A. W. Irwin, B. Campbell, C. L. Morbey, G. A. H. Walker, and S. Yang. Long-period radial-velocity variations of Arcturus. , 101:147–159, Feb. 1989. doi: 10.1086/132415.

C. M. Johns and G. Basri. Hamilton Echelle Spectra of Young Stars. II. Time Series Analysis of H(alpha) Variations. , 109:2800, June 1995. doi: 10.1086/117487.

C. M. Johns-Krull and G. Basri. The Spectral Variability of the T Tauri Star DF Tauri. , 474:433–454, Jan. 1997. doi: 10.1086/303460.

C. M. Johns-Krull and J. A. Valenti. New Infrared Veiling Measurements and Constraints on Accretion Disk Models for Classical T Tauri Stars. , 561:1060–1073, Nov. 2001. doi: 10.1086/323257.

M. T. Karim, K. G. Stassun, C. Briceño, A. K. Vivas, S. Raetz, C. Mateu, J. José Downes, N. Calvet, J. Hernández, R. Neuhäuser, M. Mugrauer, H. Takahashi, K. Tachihara, R. Chini, G. A. Cruz-Dias, A. Aarnio, D. J. James, and M. Hackstein. The Rotation Period Distributions of 4-10 Myr T Tauri Stars in Orion OB1: New Constraints on Pre-main-sequence Angular Momentum Evolution. , 152:198, Dec. 2016. doi: 10.3847/0004-6256/152/6/198.

S. J. Kenyon, D. Dobrzycka, and L. Hartmann. A new optical extinction law and distance estimate for the Taurus-Auriga molecular cloud. , 108:1872–1880, Nov. 1994. doi: 10.1086/117200.

S. Kim, L. Prato, and I. McLean. REDSPEC: NIRSPEC data reduction. Astrophysics Source Code Library, July 2015.

A. L. Kraus, M. J. Ireland, D. Huber, A. W. Mann, and T. J. Dupuy. The Impact of Stellar Multiplicity on Planetary Systems. I. The Ruinous Influence of Close Binary Companions. , 152:8, July 2016. doi: 10.3847/0004-6256/152/1/8.

F. K. Lamb, J.-J. Aly, M. C. Cook, and D. Q. Lamb. Synchronization of Magnetic White Dwarfs in Close Binary Systems. In D. Q. Lamb and J. Patterson, editors, *Cataclysmic Variables and Low-Mass X-ray Binaries*, volume 113 of *Astrophysics and Space Science Library*, page 237, 1985. doi: 10.1007/978-94-009-5319-2_25.

N. R. Lomb. Least-squares frequency analysis of unequally spaced data. , 39:447–462, Feb. 1976. doi: 10.1007/BF00648343.

G. N. Mace, L. Prato, G. Torres, L. H. Wasserman, R. D. Mathieu, and I. S. McLean. Dynamical Measurements of the Young Upper Scorpius Triple NTTS 155808-2219. , 144:55, Aug. 2012. doi: 10.1088/0004-6256/144/2/55.

I. S. McLean, E. E. Becklin, O. Bendiksen, G. Brims, J. Canfield, D. F. Figer, J. R. Graham, J. Hare, F. Lacayanga, J. E. Larkin, S. B. Larson, N. Levenson, N. Magnone, H. Teplitz, and W. Wong. Design and development of NIRSPEC: a near-infrared echelle spectrograph for the Keck II telescope. In A. M. Fowler, editor, *Infrared Astronomical Instrumentation*, volume 3354 of , pages 566–578, Aug. 1998. doi: 10.1117/12.317283.

I. S. McLean, J. R. Graham, E. E. Becklin, D. F. Figer, J. E. Larkin, N. A. Levenson, and H. I. Teplitz. Performance and results with the NIRSPEC echelle spectrograph on the Keck II telescope. In M. Iye and A. F. Moorwood, editors, *Optical and IR Telescope Instrumentation and Detectors*, volume 4008 of , pages 1048–1055, Aug. 2000. doi: 10.1117/12.395422.

E. E. Mendoza. Additional Infrared Photometry of T Tauri Stars and Related Objects. , 72:816, Sept. 1967. doi: 10.1086/110554.

P. P. Petrov. Multicolor television photometry of T Tauri stars. I - Observational technique and preliminary results. II - The nature of variability in T Tauri stars. *Izvestiya Ordena Trudovogo Krasnogo Znameni Krymskoj Astrofizicheskoj Observatorii*, 54:42–84, 1976.

G. Pojmanski. The All Sky Automated Survey. , 47:467–481, Oct. 1997.

G. Pojmanski. VizieR Online Data Catalog: All Sky Automated Survey Catalog (Pojmanski+, 2000). *VizieR Online Data Catalog (other)*, 50, Sept. 2005.

D. Raghavan, H. A. McAlister, T. J. Henry, D. W. Latham, G. W. Marcy, B. D. Mason, D. R. Gies, R. J. White, and T. A. ten Brummelaar. A Survey of Stellar Families: Multiplicity of Solar-type Stars. , 190:1–42, Sept. 2010. doi: 10.1088/0067-0049/190/1/1.

M. Richter, G. Basri, S. Perlmutter, and C. Pennypacker. Automated CCD photometry of T Tauri stars. , 104:1144–1151, Dec. 1992. doi: 10.1086/133101.

L. Rigon, A. Scholz, D. Anderson, and R. West. Long-term variability of T Tauri stars using WASP. , 465:3889–3901, Mar. 2017. doi: 10.1093/mnras/stw2977.

A. E. Rydgren, D. S. Zak, F. J. Vrba, P. F. Chugainov, and G. V. Zajtseva. UBVRI monitoring of five late-type pre-main-sequence stars. , 89:1015–1021, July 1984. doi: 10.1086/113597.

J. D. Scargle. Studies in astronomical time series analysis. II - Statistical aspects of spectral analysis of unevenly spaced data. , 263:835–853, Dec. 1982. doi: 10.1086/160554.

G. H. Schaefer, M. Simon, E. Nelan, and S. T. Holfeltz. Dynamical Masses of Young Stars in Multiple Systems. , 126:1971–1980, Oct. 2003. doi: 10.1086/378055.

G. H. Schaefer, M. Simon, T. L. Beck, E. Nelan, and L. Prato. Dynamical Mass Estimates for Incomplete Orbits: Young Multiple Stars in Taurus and Ophiuchus. , 132:2618–2633, Dec. 2006. doi: 10.1086/508935.

G. H. Schaefer, L. Prato, M. Simon, and R. T. Zavala. Orbit and Stellar Properties of the Young Triple V807 Tau. , 756:120, Sept. 2012. doi: 10.1088/0004-637X/756/2/120.

G. H. Schaefer, L. Prato, M. Simon, and J. Patience. Orbital Motion in Pre-main Sequence Binaries. , 147:157, June 2014. doi: 10.1088/0004-6256/147/6/157.

A. F. Shajmieva and N. A. Shutemova. Two years photoelectric UBVR observations of DF and DG Tauri. *Peremennye Zvezdy*, 22:176–179, 1985.

D. Shakhovskoj, V. Grinin, A. Rostopchina, D. Schertl, K.-H. Hofmann, G. Weigelt, Y. Balega, O. Kiyaeva, and S. Melnikov. Photopolarimetric activity and circumstellar environment of the young binary system DF Tau. , 448:1075–1082, Mar. 2006. doi: 10.1051/0004-6361:20053936.

V. S. Shevchenko and N. A. Shutyomova. The Search of the Short-Time Light Variations in Df-Tauri. *Astrofizika*, 17:509, July 1981.

F. H. Shu, F. C. Adams, and S. Lizano. Star formation in molecular clouds - Observation and theory. , 25:23–81, 1987. doi: 10.1146/annurev.aa.25.090187.000323.

J. Smak. On the colors of T Tauri stars and related objects. , 139:1095, May 1964. doi: 10.1086/147851.

K. G. Stassun, R. D. Mathieu, T. Mazeh, and F. J. Vrba. Examining the case for regulation of pre-main-sequence rotation by circumstellar disks. In R. Pallavicini, G. Micela, and S. Sciortino, editors, *Stellar Clusters and Associations: Convection, Rotation, and Dynamos*, volume 198 of *Astronomical Society of the Pacific Conference Series*, page 309, 2000.

J. A. Valenti and C. M. Johns-Krull. Observations of Magnetic Fields on T Tauri Stars. , 292:619–629, Aug. 2004. doi: 10.1023/B:ASTR.0000045068.34836.cf.

C. Varsavsky. Three color photometry of T Tauri stars. *Boletin de la Asociacion Argentina de Astronomia La Plata Argentina*, 3:6, 1961.

S. N. Vogel and L. V. Kuhi. Rotational velocities of pre-main-sequence stars. , 245: 960–976, May 1981. doi: 10.1086/158872.

B. von Rekowski and N. Piskunov. Global 3-D solar-type star-disc dynamo systems: I. MHD modeling. *Astronomische Nachrichten*, 327:340, May 2006. doi: 10.1002/asna.200510526.

F. M. Walter. The naked T Tauri stars - The low-mass pre-main sequence unveiled. , 99:31–37, Jan. 1987. doi: 10.1086/131952.

R. J. White and A. M. Ghez. Observational Constraints on the Formation and Evolution of Binary Stars. , 556:265–295, July 2001. doi: 10.1086/321542.

G. V. Zaitseva and V. M. Liutyi. Photometry with 10-sec resolution for the T Tauri variable DF Tauri. *Soviet Astronomy Letters*, 2:167–169, Oct. 1976.

M. Zechmeister and M. Kürster. The generalised Lomb-Scargle periodogram. A new formalism for the floating-mean and Keplerian periodograms. , 496:577–584, Mar. 2009. doi: 10.1051/0004-6361:200811296.